KFA

KERNFORSCHUNGSANLAGE JÜLICH GmbH

Institut für Festkörperforschung

Characterization of the high temperature fracture of He-implanted 1.4970 austenitic stainless steel

by

A. A. Sagüés

Jül - 1409
März 1977

Als Manuskript gedruckt
ISSN 0366-0885

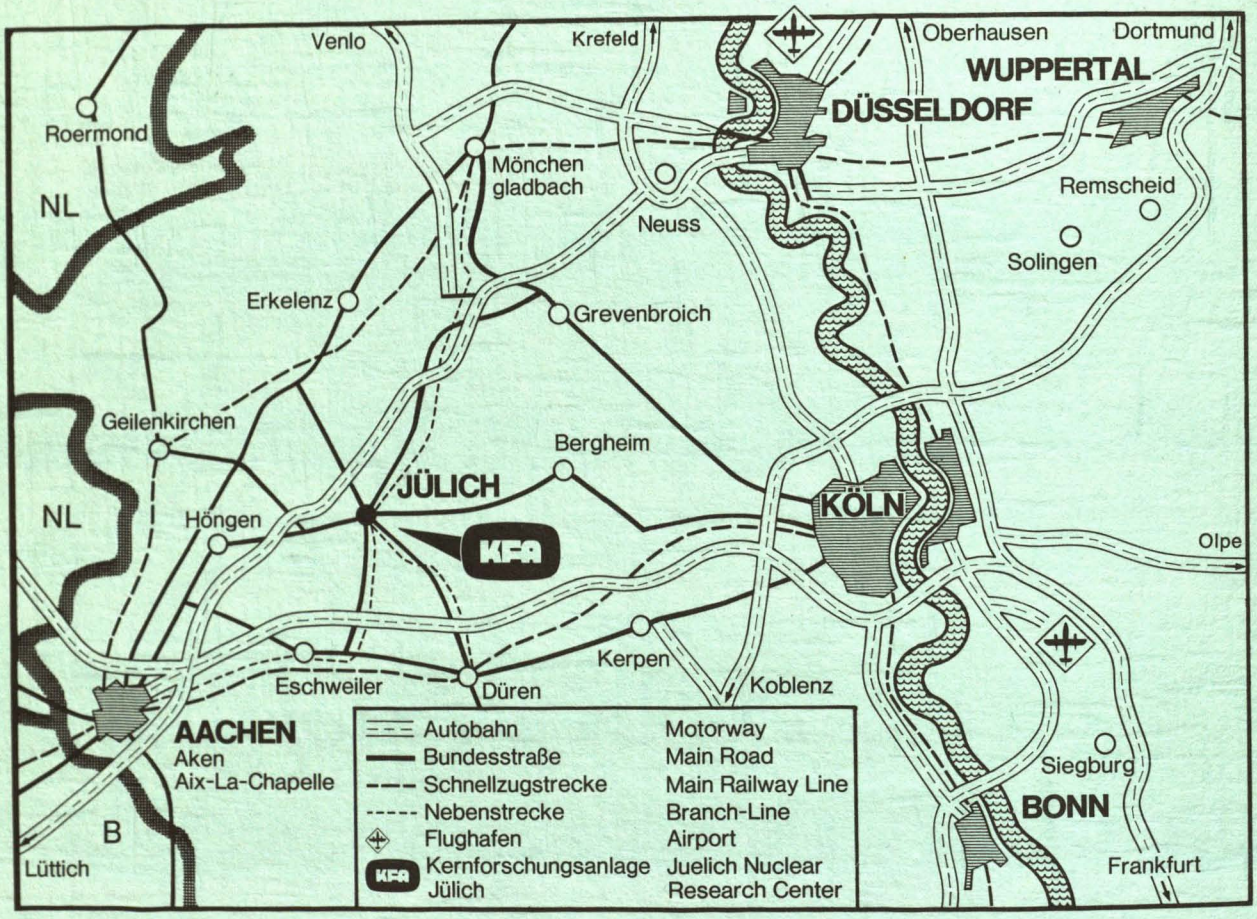

Berichte der Kernforschungsanlage Jülich - Nr. 1409

Institut für Festkörperforschung Jül - 1409

Im Tausch zu beziehen durch: ZENTRALBIBLIOTHEK der Kernforschungsanlage Jülich GmbH, Jülich, Bundesrepublik Deutschland

Characterization of the high temperature fracture of He-implanted 1.4970 austenitic stainless steel

by

A. A. Sagüés

FOREWORD

The results presented here correspond to the first stage of an investigation presently being conducted at the Institut für Festkörperforschung, KFA Jülich on the He embrittlement of metals.

The author is indebted to H. Ullmaier for his valuable advice during the investigation and help in the preparation of the manuscript, to J. Auer and P. Jung for their generous collaboration and support during the author's stay in Jülich, and to T. Schober for his introduction to the electron microscopy techniques.

The experiments would not have been possible without the cooperation of the Institut für Kernphysik, KFA Jülich by permitting the use of the JULIC cyclotron for the He implantations. The sample material, together with much useful information was provided by W. Dietz of INTERATOM GmbH.

ABSTRACT

The Ti-stabilized DIN 1.4970 austenitic stainless steel is an important candidate for high temperature - high neutron fluence applications which will create appreciable amounts of He within the matrix. In order to determine the mechanical effects associated with the presence of He alone a set of tensile specimens was cyclotron implanted to uniform He concentrations in the 10^{-6} to 10^{-4}/at. range and later creep tested at 700 and 800°C. It was found that the elongation to fracture values of the implanted specimens were reduced with respect to those of unimplanted controls. Scanning electron microscope examination revealed that fracture starts as intergranular and subsequently propagates in a transgranular fashion, the intergranular part being much more extended in the implanted material. Cavities appearing in the fractured grain boundaries of the implanted specimens were associated with grain boundary chromium carbide precipitates. Transmission electron micrsocope examination of the creep specimens and of foils annealed at temperatures between 800 and 1000°C after implantation revealed that He segregated as bubbles in the matrix, at the grain boundaries and at intergranular precipitates.

A mechanism of He induced cavitation is discussed which accounts for the observed loss of ductility. Changes in the mode of crack propagation during fracture are attributed to geometrical factors and tensile loading characteristics.

INTRODUCTION

The presence of insoluble gases created within metals as a result of neutron irradiation has long been identified as one of the causes of high temperature embrittlement of alloys used in reactor applications. Most of the research done up to now (see Refs. 1 and 2 for reviews) agrees in that the effect is

1. Mainly the result of the nuclear reaction product, He.
2. Already significant after a few atomic ppm of He are present in the material.
3. Occurring at high temperatures (i.e. $\gtrsim$ of melting temperature) and low strain rates.
4. Characterized by intergranular fracture.

The mechanism by which ductility is lost is understood only partially and may vary for different materials or different conditions of a given material. Although a sizeable body of research has been carried out for the case of the austenitic steels it is not yet possible to accurately predict how a particular alloy will behave once He is introduced. The problem is of special importance in the case of fuel cladding elements and other core components in fast breeder and future fusion reactors.

For the German SNR fast breeder reactor (3) the alloys DIN 1.4970 is a first candidate for the core components. This is a Ti-stabilized austenitic stainless steel with the composition given in Table I. The SNR concept foresees operating temperatures at the cladding elements as high as 620°C and the possibility of localized spots reaching 710°C (4). A total neutron dose of up to $1.2\ 10^{23}$ n/cm^2 (> 0.1 MeV) is expected and can result in He being produced through (n,α) reactions at a rate of around 10 at ppm/year.

Several experiments have been conducted to date on the fracture behavior of the alloys after neutron irradiation in experimental fast reactors (5, 6), producing He concentrations in the range of interest. Although these results provide valuable information on the overall effects of radiation and on the technical feasibility of the alloy, they hardly lead to an understanding of

the embrittling effect itself. It is therefore of interest to isolate the effects which are caused by the presence of He alone. This would allow an unobscured observation of the phenomenon and provide a better chance of determining which parameters may be varied to make the alloy less sensitive to high temperature embrittlement.

Cyclotron implantation by means of a variable energy beam provides a fast and convenient way of introducing He with a minimum of side effects: a few hours of irradiation can result in uniform He concentrations that would require years of reactor exposure to be achieved (7).

It is the purpose of the present study to take advantage of this technique in order to 1. Gain additional information on the fracture behavior of the alloy 1.4970 when loaded with amounts of He similar to those expected during service and 2. Achieve a better understanding of the mechanisms by which insoluble gases produce high temperature embrittlement.

EXPERIMENTAL

Figure 1 shows the experimental sequence followed. The starting material was provided by Interatom GmbH and consisted of actual SNR-300 Mark 2 (3) fuel pin tubes, 7.6 mm diameter and 0.5 mm wall thickness. These tubes were made by Sandvik of Sweden under the denomination 12R72HV. Their chemical composition as provided by the manufacturer is given in Table I.

The tubes were split longitudinally and then cold rolled to a thickness of 120 μm (∿ 75 % cold work). The stripes so obtained were then solution trated for 1 hr. at 1100°C and afterwards cold rolled again to a thickness of 105 μm (∿ 13 % cold work). Foil tensile specimens with the dimensions given in Figure 2 were spark cut from the stripes and subsequently aged for 24 hours. at 800°C. The material so treated is defined to be in the standard condition. This condition was chosen to be similar to that used in previous investigations (6) in order to facilitate direct comparison with published data. All the thermal tratements described above were done at a vacuum of 10^{-5} torr.

He implantations were done with the AEG isocron-cyclotron of the Institut für Kernphysik, KFA Jülich using the arrangement shown schematically in Figure 3. A defocused α-particle beam of 100 MeV initial energy was swept along each specimen while its energy was being varied by continuosly moving the interposed, water cooled aluminium wedge. The excursion of the wedge was adjusted so as to obtain penetration ranges varying from zero to just above the thickness of the specimen being implanted. Uniform He deposition through and along the specimen was thus achieved. Once one specimen was finished a steering magnet shifted the beam to the next. The 0.7 mm thick plate A made out of copper served as a final energy degrader. The temperature of the specimen was held steady at 50°C by pressing it between plate A and the water cooled block B. The irradiation current and time were adjusted to obtain He deposition rates of 4-8 at ppm/hr and final concentrations between 1 and 80 at ppm. The implantation chamber was kept at a vacuum of ∿ 10^{-5} torr.

After implantation some of the samples were tensile tested at a strain rate of $1.5\ 10^{-4}$/sec. The test were performed in a He atmosphere with an estimated O_2 partial pressure of 2.10^{-7} torr and at temperatures of 20, 750 and 800°C. The specimens were kept at the test temperature for at least 20 min before applying a load.

Other samples underwent creep tests which followed the general arrangement used by Morikawa (8). The tests involved creep under constant stress conditions (but only for that part of the test in which the specimen was uniformely deformed) which were achieved by means of a spring loading system. The strain was recorded continuously; all the tests were performed on a vacuum of $\sim 5.10^{-7}$ torr. A sensor was set to turn off the oven immediately after fracture in order to minimize contamination of the freshly exposed fractured surface. Most of the tests were conducted at strain rates in the order of 3.10^{-4}/hr, and at temperatures of 700 and 800°C. Because of the small specimen dimensions and other geometrical limitations the initial tensile stress was measured with an accuracy of $\pm$ 3 % which, together with the low strain hardening of the alloy at the creep testing temperatures results in the significant dispersion of the creep data that will be shown later.

Transmission Electron Microscopy (TEM) samples were made by electrolytic thinning of the specimens in a Tenupol dual jet machine. A 10 % Perchloric acid, 90 % Acetic acid solution operated at 11°C and 70 V gave satisfactory results. Pulsing the current at $\sim$ 1 Hz with a duty cycle of 50 % prevented overheating of the polishing cell. TEM examinations were made with a Philips EM 300 microscope operated at 100 kV. Features such as He bubbles had a detection limit of $\sim$ 30 Å in well annealed specimens.

The fracture and other surface features of the specimens were examined (without preparation treatements) with a Philips PSEM 500 Scanning Electron Microscope (SEM) operated at 12.5 to 50 kV. Deep etching with a solution of 50cc HCl, 5cc NO_3H and 50 cc H_2O for a few minutes at 50°C was used in one instance

to reveal the precipitate structure of the material. An EDAX X-Ray spectrum analyzer attached to the SEM was used to provide qualitative composition information of features.

RESULTS

MICROSTRUCTURE

The material in the standard condition had an average grain size of $\sim$ 30 μm with roughly one to two twinning regions per grain. This results in $\sim$ 5 bidimensional discontinuities per specimen thickness. Figure 4 shows an SEM picture of the surface of an specimen which was polished and deep-etched. The rhomboidal, 6 μm wide feature is a Ti carbide precipitate. This type of precipitates are far apart from each other (typically 100 grain diameters) and serve as stabilizers by taking some carbon out of solid solution. The aligned features in white, $\sim$ 1 μm are almost entirely chromium-rich precipitates, most likely carbides located along the grain boundaries. Figure 5 is a TEM picture showing this type of precipitate in detail. The large density of dislocations is evident despite the intentional off-contrast condition. The density of precipitates at twin boundaries was an order of magnitude lower than that of the grain boundaries. No evidence of martensite or large scale departure from an austenitic matrix was observed in the material on the standard condition or after subsequent tests.

TENSILE TESTS

Figure 6 shows load-elongation diagrams of implanted and control specimens obtained at a strain rate $\dot{\varepsilon} = 1.5.10^{-4}$ sec^{-1}. The results of these preliminary tests are summarized in Table II.

At $20^{o}C$ strain hardening occurrs and deformation bands are observable along the whole gage length of the specimen. The abrupt end at the right of the curve is characteristic of foil specimens; Ref. (9) deals with this phenomenon in more detail.

At $750^{o}C$ and $800^{o}C$ the yield stress and elongation to fracture become lower. A tendency to serrated flow and negative strain hardening as the temperature increases is apparent for both the implanted and unimplanted material. At the same time the deformation bands are localized around the central 1/3 of the gage length.

The specimens loaded with 8 at ppm He presented a higher yield stress and a lower (especially at 800°C) elongation to fracture (see Fig. 6).

CREEP TESTS

The mechanical parameters and results of the creep experiments are listed in Table III. Figure 7 shows typical elongation-time curves for the control and implanted specimens tested at 700°C. The primary creep stage was of short duration. The secondary creep region is not well defined and in some specimens was non-existent. The implanted specimens reached fracture before pronounced tertiaty creep could develope.

A rough evaluation of the speed at which a test was conducted can be done by defining an average strain rate $\bar{\dot{\varepsilon}}$ as:

$$\bar{\dot{\varepsilon}} = \frac{\text{strain to fracture}}{\text{time to fracture}}$$

Figure 8 shows the range of $\bar{\dot{\varepsilon}}$ values obtained at 700°C as a function of the initial tensile stress. The data of Ref. (6), resulting from specimens with approximately the same standard condition but different geometry are overimposed showing compatibility within the experimental limits.

Figure 9 is a plot of the elongation to fracture and the applied stress as a function of time to fracture for those specimens tested at 700°C. The specimens loaded with more than 1 at ppm He have an average elongation to fracture $\sim$ 3 times smaller than that of their controls. The stress-time data reveals a high sensitivity of the time to fracture to the applied stress, which obscures the effect of implantation on this relationship.

Figure 10 presents elongation to fracture at 700°C as a function of the amount of He implanted.

Some preliminary creep tests at 800°C are also listed in Table III. The general shape of the creep curves at that temperature resembles that shown in Figure 7. Values of $\bar{\dot{\varepsilon}}$ comparable to those measured at 700°C were reached at considerably lower stresses.

The average elongations to fracture of control and implanted specimens at both temperatures, and within the 15 to 30 at ppm He concentration range are compared in Table IV.

SCANNING ELECTRON MICROSCOPY

Creep specimens

During the high temperature creep experiments the foil specimens fractured in the manner shown schematically in Figure 11. A crack originates at one of the foil's edges and propagates more or less perpendicular to the tensile stress axis until reaching the opposite end. In most unimplanted specimens the fracture is totally transgranular and chissel-like. In some cases a few (1 to 5) intergranular facets are visible at the start side of the crack, as is exemplified in Figure 12.

The implanted specimens, on the other hand, begin cracking always in a clearly intergranular fashion (see Figure 13) and the crack stays intergranular for a sizeable fraction of the specimen's width. This fraction, expressed in percents, will be called % intergranular fracture hereafter. The crack switches then to a transgranular mode and propagates as such until reaching the opposite edge of the specimen.

Figures 14 and 15 compare the appearance of the fracture surface of an unimplanted specimen observed from the direction B (Figure 11) with that of an implanted specimen seen from A (Figure 11). Figure 16 illustrates an area near the transition from intergranular to the transgranular mode.

Figure 17 is a plot of % intergranular fracture as a function of the implanted He content for the specimens creep tested at 700°C. The limit bar represents the upper value measured for unimplanted specimens; this value is almost coincident with that of the specimen with the lowest implanted He content (1 at ppm).

Table V shows that for the 15 to 30 at ppm He concentration range covered by the preliminary 800°C data the average % intergranular fracture values are significantly larger than those measured at 700°C.

The detailed appearance of the material is listed below for the two test temperatures.

700°C: The intergranular fracture surface of a He implanted specimen seen at high magnification (Figure 18) presents convex and concave features ∿ 1-2 μm in size separated by about that same distance from each other. Certain grain facets (A) present a clear separation between the convex features and their background. Others (B) look more crowded and it is difficult to recognize the character of individual features. The X-ray spectrum excited with a 12.5 kV electron beam (sampling depth ∿ 5 μm) revealed that features as those indicated by arrows are several times richer in Cr than the background.

The side surfaces of the specimens show evidence of unevenly distributed plastic deformation. In some cases less than 30 % of the gage length presented observable surface deformation.

Usually only one crack developed across the samples, but in a few specimens such as the one shown in Figure 19 it was possible to see a second, almost fully developed crack. This specimen contained 15 at ppm He; the upper crack started as intergranular in the left and propagated towards the right edge. The lower crack started from the right in the same way but the tensile stress dropped before its completion. For both cracks the magnitude % Intergranular fracture is ∿ 10-20. Figure 20 is a close-up of the advancing, already transgranular lower crack. Surface deformation bands are visible on some of the grains. Several short cracks can be seen between the grains; these shallow cracks appear in both implanted and unimplanted specimens and seem to be only a few microns deep. They become wider near the main crack. Figure 21 is a stereo pair illustrating these characteristics in detail, this time for the case of an unimplanted specimen.

Another type of short crack observed on the side surfaces can be seen as a short black line in the upper part of Figure 19. Figure 22 shows that crack and its surroundings in more detail. The stereo pair of figure 23 reveals that this type of crack is deep and with grain boundary features similar to those shown

in Figure 18. These short, deep cracks were seen only in a few implanted specimens, and not observed at all in the unimplanted material.

800°C: The stereo pair of Figure 24 shows the intergranular part of the fracture of a specimen loaded with 15 at ppm He. A large number of concave features is visible. Figure 25 is a close-up showing some of the convex features also present. Analysis of the X-ray spectrum identifies again the particles as Chromium-rich, including the elongated ones in the lower left center. Figure 26 shows the structure of a fracture-exposed grain facet. The stress axis was inclined with respect to this surface. The structure is almost cellular, with Chromium-rich particles located inside some of the concave features. Figure 27 shows a row of cavities appearing in the intergranular part of the fracture of a specimen loaded with 30 at ppm He.

The side surface of the specimens tested at 800°C had the same general appearance of the 700°C material. A deep secondary crack (Figure 28) allowed the examination of its tip in detail (Figure 29). Chromium-rich particles are seen adhered to the opening sides.

Tensile-test specimens

The unimplanted material tested at 20, 750 and 800°C had completely transgranular, dimpled fracture surfaces.

The He-implanted specimens presented only 2 to 3 grain facets at the beginning of the fracture crack, the rest of it being transgranular. Figure 30 shows the intergranular part of the fracture of a specimen loaded with 8 at ppm He and tested at 800°C. Most of the exposed particles are Chromium-rich; in some places particles and concave features appear to be associated.

TRANSMISSION ELECTRON MICROSCOPY

Qualitative TEM examination of the implanted specimens that underwent creep at 700°C revealed little difference between them and the undeformed material in the standard condition. Specimens implanted with He and creep tested at 700°C failed to show qualitative differences with their unimplanted controls. No evidence of He segregation in the form of bubbles was found in that case. However, the large density of dislocations already present in the standard condition precluded the observation of bubbles or cavities smaller than $\sim$ 50 Å in diameter in most of the usable specimen area. Because of the polishing technique used, the transparent area was always located at a distance of at least 1 mm from the main fracture crack.

The unimplanted material creep tested at 800°C showed again no marked difference with that on the standard condition. The specimens implanted with 15 at ppm He and creep tested at 800°C showed grain boundary cavities, $\sim$ 50 Å in diameter, which imaged in a manner typical of He bubbles. These cavities were far apart (typically $\sim$ 1 per intersected grain boundary facet, when using a nominal specimen thickness of 2000 Å) and their size or density seemed to be independent of the distance between the transparent area and the main fracture crack. The specimen which was loaded with 30 at ppm He and creep tested at 800°C presented larger cavities ($\sim$ 100 Å in diameter). These seemed to appear only in some parts of the transparent area and an estimation of their number density was difficult.

Table VI summarizes these observations.

Some as-implanted specimens were annealed in the absence of stress for a time of 1 hr and later examined in the TEM. Table VII summarizes these results. The microstructure of the standard condition was not visibly altered after the anneals at 700° or 800°C. Appreciable amounts of recovery were observed after the 900 and 1000°C anneals.

He bubbles were detected for some specimens already after annealing at 800°C. The estimated bubble number density was higher in the specimens annealed at higher temperatures. Table VII lists in order of decreasing preference the location of bubbles. Bubbles at the junction of three grain boundaries were common. In one instance (Figure 31) a group of bubbles was associated with linear features having the general contrasting behavior of grain boundary dislocations. Examples of bubbles associated with grain boundary precipitates and with free dislocations are shown in Figure 32 and Figure 33. Only a small fraction (i.e. $\sim 10^{-2}$) of the bubbles in any specimen appeared to be in the matrix, unassociated with other features. The average bubble size did not appear to change with temperature and concentration as much as the bubble number density did.

DISCUSSION

SPECIMEN GEOMETRY AND MECHANICAL BEHAVIOR

The $\sim$ 100 μm thin foil format of the specimens was chosen as a result of a compromise between factors such as the α particle penetration range, the tensile load capability of the mechanical test equipment, a practical grain size, and the relative importance of surface effects when trying to extrapolate results to bulk material. The interplay between those parameters has been discussed in a previous paper (9), in which is reported that for the case of foil specimens of "pure" 316 stainless steel (10) a ratio $D/d \geq 2.5$ (where D is the foil thickness and d is the average grain size) is enough to result in yield and ultimate tensile stress values which are equal to those measured in the bulk material. The same paper shows that surface contamination may reduce significantly the creep rate of foil specimens during high temperature tests. As a result, in the present investigation a D/d ratio of at least 5 was adopted, and in order to minimize surface oxidation the creep tests were performed in vacua better than 5.10^{-7} torr.

An inspection of the stress elongation curves (Figure 6) reveals that at the higher temperatures the flow stress drops as the material is deformed. This correlates well with the virtual absence of secondary creep at the same high temperatures since the condition described above would favor an early onset of tertiary creep. The question arises whether this behavior is a result of a true negative strain hardening coefficient determined by the physical condition of the material, or a result of the geometrical effects mentioned earlier and not completely cancelled. The latter case would occur, for example, if grain rotation during plastic deformation would still produce large and localized reductions of area which in turn result in early plastic instability even in a material with a positive strain hardening coefficient. However, (1) in a separate investigation (11) larger tubular specimens of the same alloy, and thus more representative of the bulk condition, showed negligible work hardening during the early stages of plastic deformation in the

700°C - 800°C range, and (2) the foil specimen which was tested at 20°C (Table II) having exactly the same shape as those tested at 750°C and 800°C, produced a well defined, positive-slope load elongation curve. These observations indicate the likelihood of a real decrease of the strain hardening coefficient with increasing temperature, the geometrical factors playing only a secondary role.

EFFECT OF IMPLANTED He ON THE MECHANICAL BEHAVIOR

Hardening. The limited data of the tensile tests (Table II) show an increase of the high temperature flow stress after He implantation. The small amount of radiation damage incurred during implantation (10^{-2} to 10^{-3} dpa) is in all probability annealed out during the pre-test anneal at the test temperature and can therefore not account for the observed hardening. Therefore, the nardening seems to be due to the pinning of otherwise mobile dislocations by He bubbles.

The experimental limitations of the creep tests obscure any small effect of the presence of He on the material hardness or the creep rate. The lower creep rate apparent for the implanted specimen in Figure 7 when compared with that of the unimplanted control is well within the experimental scatter. The clustering of $\dot{\varepsilon}$ values of the implanted specimens at a lower level than that of their controls (Figure 8) is a consequence of shorter tertiaty creep and not of systematically different initial creep rates.

Ductility. The plastic instability discussed earlier accounts for the noticeable dispersion of the total elongation values reported. The other ductility parameter used here, % intergranular fracture, can be interpreted as a reciprocal indication of the reduction in area during fracture. Both parameters show that a large detrimental effect of He on ductility (at 700°C) is produced already by 5 at ppm He, whereas at 800°C the amount of He required for such effect may even be smaller. Because of the specimen geometry and the way in which fracture propagates it becomes difficult to determine whether saturation of the effect as a function of Helium content is achieved at all, and

in which conditions it would happen. The two parameters used here seem to saturate at $\sim$ 30 at ppm He on the 700°C tests.

Fracture propagation. The intergranular crack started at one of the foil's edges results in an increased tensile stress in the remainder of the cross section. The crack will therefore propagate with increasing speed until a strain rate is reached that results in a change of fracture mechanism, evidenced by the transition from intergranular to transgranular tearing. It follows that the appearance of the fracture surface and parameters such as the elongation to fracture will then be sensitive to the specimen geometry, the test assembly stiffness and whether the test is performed at constant nominal stress or at a constant strain rate. All these factors should be taken into account in future attempts to determine which levels of He concentration are necessary to saturate the embrittling effect.

MECHANISM OF EMBRITTLEMENT

In 1965 Barnes (12) proposed a mechanism of He embrittlement based in the observation that He precipitates at the grain boundaries of metals in which it has been implanted. This precipitation is in the shape of bubbles and takes place at temperatures that are high enough to create an abundant supply of vacancies at the grain boundaries. If a tensile stress σ is then applied in a direction perpendicular to the grain boundary the He bubbles will grow to achieve a thermodynamical equilibrium between the internal gas pressure, the external stress and the interface energy. If the external stress exceeds the critical value

$$\sigma_c \gtrsim 0.77 \frac{\gamma}{r} \qquad (1)$$

where r = original bubble radius
γ = interface energy

the bubble will grow in an unrestricted fashion, without being able to reach equilibrium. Figure 34 is a plot of the critical condition in which a value γ = 1000 erg cm^{-2}, representative of the material being investigated, has been used.

The unrestricted bubble growth will ultimately result in the linking of adjacent growing bubbles and the generation of an intergranular crack. The embrittling effect will be more noticeable the larger the number of critical size bubbles present per unit surface at the grain boundaries.

The results presented in the previous section suggest that such a mechanism of He-induced cavitation is responsible for the observed loss of ductility, and that at least part of the cavities are generated at the already existing grain boundary precipitates. Qualitative considerations supporting that interpretation are that 1) the large number of concave features that appear at the grain boundary facets (conspicuous in Figure 24), the strings of features apparent in Figures 27 and 30, and the appearance of the crack tip shown in Figure 29 are all characteristic of the appearance of a material that failed by intergranular cavitation (13); 2) the average distance between cavities, both at 700°C and 800°C is of the same order as the separation between grain boundary precipitates; 3) cavities can be seen to be associated with precipitates in the examples of Figure 2o and possibly in the string of Figure 30; 4) bubbles are seen attached to grain boundary precipitates (Tables VI and VII, Figures 32 and 33); 5) long time creep experiments with tubular specimens (11) terminating in intergranular cavitation indicate tnat tne unimplanted material is prone to this failure mode. A low precipitate-matrix adherence can account for both the initiation of cavitation in the unimplanted material and tne prefered bubble nucleation at precipitates once He is introduced.

In order for the He-induced cavitation mechanism to operate, equation (1) must be satisfied. Critical bubble sizes can be obtained from the equation or Figure 34 by inserting the creep stress values listed in Table II and assuming γ = 1000 erg/cm^2. In doing so it can be seen that in only one case (specimen # 38 tested at 800°C) bubbles equal or larger than the calculated critical size were observed in the TEM. For all the other specimens, bubble sizes were either under the $2r \sim 50$ Å detection limit (700°C specimens) or just above it (800°C specimens), and

did not satisfy the critical condition. This discrepancy is removed if the maximum stress that the matrix can sustain (namely the yield stress as determined from the tensile experiments) is used to evaluate the critical bubble size. In that case the critical size becomes $2r \sim 50$ Å at $700^{o}C$ and $2r \sim 60$ A at $800^{o}C$, in closer agreement with the TEM observations. It should be also pointed out that since bubbles tend to nucleate at precipitate-matrix interfaces the value of γ there may be lower than the assumed value of 1000 erg/cm^{-2}, and as a result a lower bubble radius would be necessary to reach the critical condition.

The choice of the yield stress as the value for σ_c takes into account the concentration of stresses existing in areas of the specimen. This occurs mainly at irregularities introduced by the spark-cutting process at the edges of the specimens. In addition one of the edges is always an area of maximum stress as a result of unavoidable misalignments of the tensile load axis. This argument is in agreement with the observation that most deep cracks originate at the specimen's edge.

SEQUENCE OF EVENTS LEADING TO CREEP FRACTURE

On the basis of the experimental results and the arguments presented above the following sequence of events can be proposed which consistently describes the process of fracture taking place in the creep experiments:

a) After the test temperature is reached He starts precipitating at the grain boundaries, probably preferentially at the already existing Cr-rich precipitates since the interface energy may be lower there.

b) He bubble growth proceeds until one or several bubbles reach the critical size. This event will tend to happen in a part of the specimen where the tensile stress is higher, perhaps as high as the flow stress. The specimen geometry, combined with the rougn finishing of spark cutting creates such a condition at the foil's edges and fracture initiates there.

c) The resulting fracture crack creates a condition of high tensile stress in the grain boundary area immediately ahead of the crack tip, which promotes to the critical condition bubbles already nucleated there. The crack will then propagate further along grain boundary lines.

d) As the load carrying cross section becomes smaller, local stresses increase and the crack propagation accelerates. After a certain crack length is reached the diffusion mechanism by which bubbles grow becomes slower than deformation by plastic flow and the path of the fracture crack becomes determined by the slip system configurations existing ahead. The fracture surface ceases being intergranular except for occassional spots (as in the case of Figure 16) wnere very favorable conditions for cavitation existed.

CONCLUSIONS

Amounts of He in excess of 5 at ppm lower the creep ductility of the alloy 1.4970 (in its standard condition) when tested at 700°C and 800°C. The extent of the embrittlement is comparable to that due to neutron irradiation producing similar He concentrations.

Examination of the microstructure and fracture surfaces suggests that the loss of ductility is due to a mechanism of He induced cavitation, in which Cr-rich intergranular precipitates serve as cavitation centers.

Specimens loaded with He present a larger intergranular fracture area than the unimplanted material. The extent of the intergranular fracture zone is determined in part by geometrical conditions, which must be taken into consideration when interpreting results from foil specimens.

BIBLIOGRAPHY

1. D.R. Harris, British Nucl. Energy Soc. Journal, 5, 74-87 (1966)

2. E.E. Bloom, Proc. Conf. on Irradiation Embrittlement and Creep in Fuel Cladding and Core Components, London, England, Nov. 9-10 1972, pp. 93-102

3. B. Hürttlen, (Editor) "Brennelemente für LWR, HTR, SNR, GSB", Jül-Conf-14, KFA Jülich (Jan. 1975)

4. H. Bergmann, B. Steinmetz, W. Dietz, Interatom Technischer Bericht ITB 75.49 (July 1975)

5. H. Bergmann (to be published)

6. Ch. Wassilew, M. Schirra, European Conference on Irradiation Behavior of Fuel Cladding and Core Component Materials, pp. 159-172, Karlsruhe, Germany (Dec. 1974)

7. R.T. King, in "Uses of Cyclotrons in Chemistry, Metallurgy, and Biology, pp. 294-315, Butterworth & Co, London (1969)

8. H. Morikawa, Jülich Report Jül-1290 (April 1976)

9. J. Auer, A. Sagüés, Proc. Intnt'l. Conf. on Radiation Effects and Tritium Technology for Fusion Reactors, Gatlinburg, Tenn., USA, Oct. 1975, Vol. II, pp. II64-II71, Eds. J. Watson and F.W. Wiffen (March 1976)

10. J.M. Leitnaker, E.E. Bloom, J.O. Stiegler, ORNL Report TM-4500, p. 2 (1974)

11. W. Dietz, private communication

12. R.S. Barnes, Nature, 206, 1307-1310 (1965)

13. A. Ruckwied, D. Ballard, Met. Trans., 3, 2999-3008 (1972)

Table I

Chemical Analysis of the Sample Material (ωt%)

C	Si	Mn	Cr	Ni	Mo	Ti	N	B	Co	Ta	Cu	V
.095	.31	1.81	15.1	15.0	1.3	.30	.01	.005	.02	.003	.02	.02

Table II

Tensile tests performed at $\dot{\varepsilon} = 1.5 \times 10^{-4}$ sec^{-1}

	Unimplanted			8 at ppm He		
Test Temperature, ^{o}C	20	750	800	20	750	800
Yield Stress, $kgmm^{-2}$	45	30	26	-	35	33
Elongation to Fracture, %	22	8	8	-	7	6

Table III

Summary of Creep Data

Specimen #	He at ppm	Test Temperature ^{o}C	Stress kg/mm^2	Time to Fracture hours	Elongation to Fracture %	$\dot{\bar{\varepsilon}}$ $x10^{4} hr^{-1}$
24			-	7	8.6	-
25			-	10	5.2	-
34			-	37	3.2	8.6
35			26.1	9	4.1	45
36			25.0	68	10.2	15
37	0	700	25.0	48	3.4	7.1
44			24.4	44	5.9	13.4
47			24.0	18.5	10.6	57
48			21.6	122	8.3	6.8
49			22.0	86	6.3	7.3
32	1		23.4	76	9.9	13
14	5		24.0	136	3.1	2.3
17	15		21.9	101	2.6	2.6
13	15		25.8	21	3.2	15
11	30	700	22.8	143	1.4	1
12	30		23.8	54	1.1	2
31	60		23.6	60	1.6	2.7
46	80		23.2	70	1.6	2.4
50			13.1	93	11.8	13
55	0	800	13.3	44	9.8	22
58			13.3	50	16	32
15	15		13.1	56	1.2	2.1
18	15	800	13.3	45	3.0	6.7
38	30		11.9	0.5	1.4	272

Table IV

Average Creep Elongation to Fracture (ETF)

Creep Temperature, ^{o}C	700	800
A = Unimplanted ETF, %	6.58	12.6
B = 15 to 30 at ppm He ETF, %	2.08	1.84
Ratio A/B	3.2	6.8

Table V

Average Creep % intergranular fracture

Creep Temperature, ^{o}C	700	800
Unimplanted	$\sim$ 0.5	$\sim$ 0.5
15 to 30 at ppm He	40	72

Table VI

Size and Location of Bubbles after Creep Tests

He at ppm	Test Temperature, ^{o}C 700	800
15	undetected	Ø ~ 50 Å GB
30	undetected	Ø 50-200 Å GB P D GBP

Key to Symbols

GB: Grain Boundaries
P : Precipitates
D : Dislocations
GBP: Grain Boundary Precipitates
GBD: Grain Boundary Dislocation
M : Matrix (Bubble is associated with no visible feature)

Table VII

Size and Location of Bubbles after 1 hr anneals

He at ppm	Annealing Temperature, ^{o}C 700	800	900	1000
30	undetected	undetected	Ø ~ 100 Å GB D GBP	Ø ~ 100 Å GB D GBP M
100	undetected	Ø 50-150 Å GB	Ø 50-150 Å GB D GBP P GBD M	

See Table VI for key to symbols

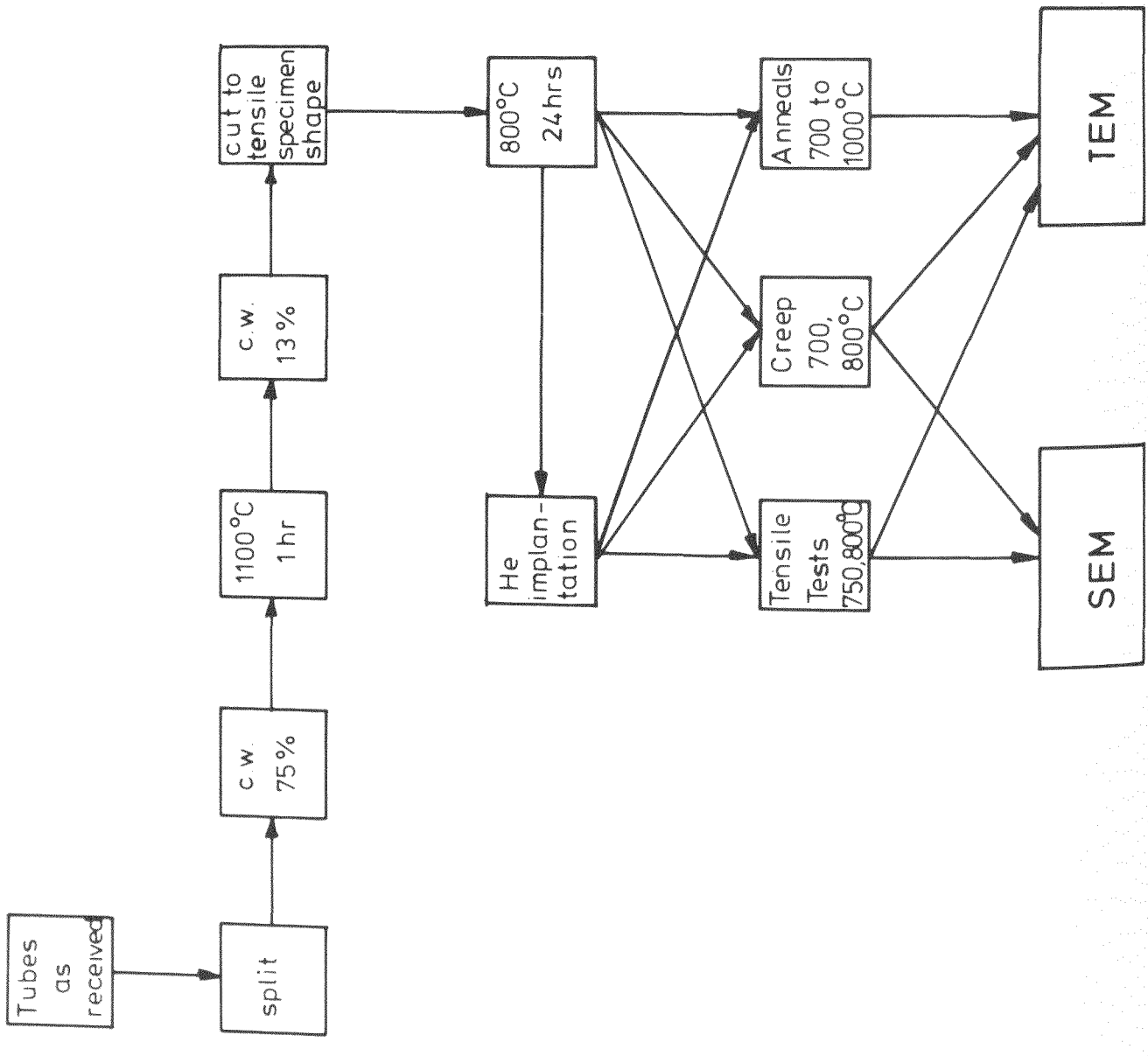

Figure 1: Experimental sequence.

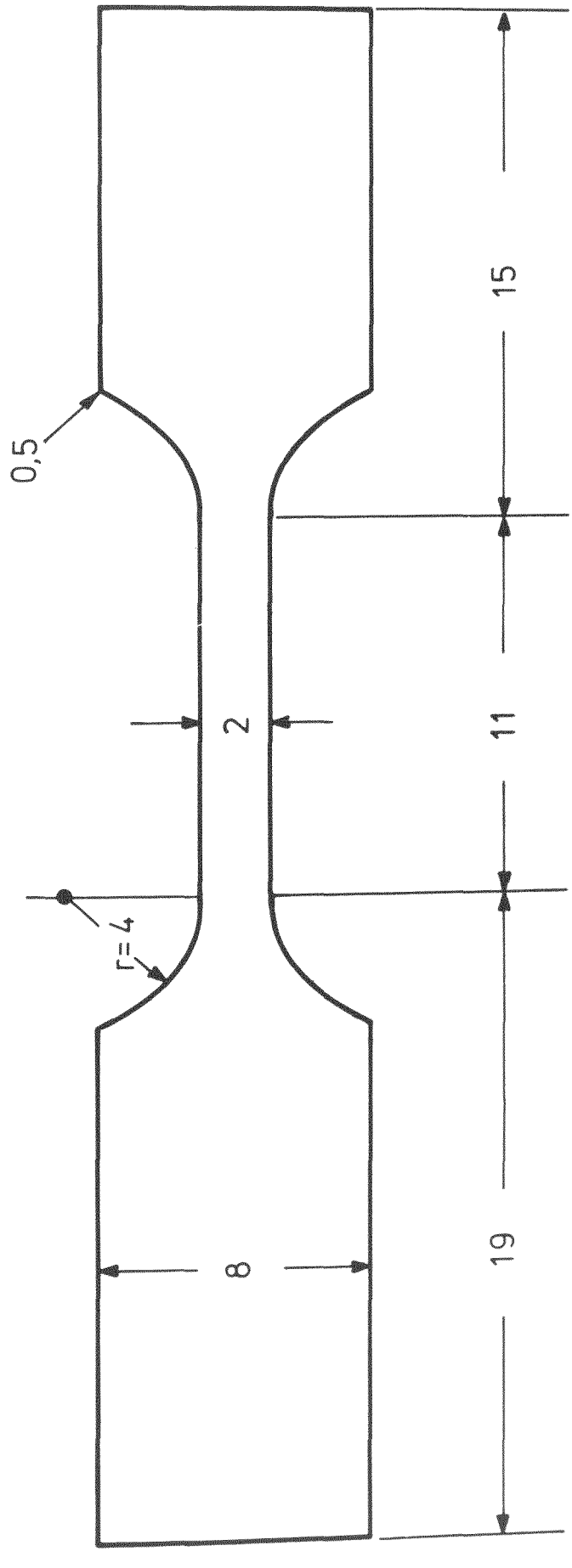

Figure 2: Mechanical specimen dimensions.

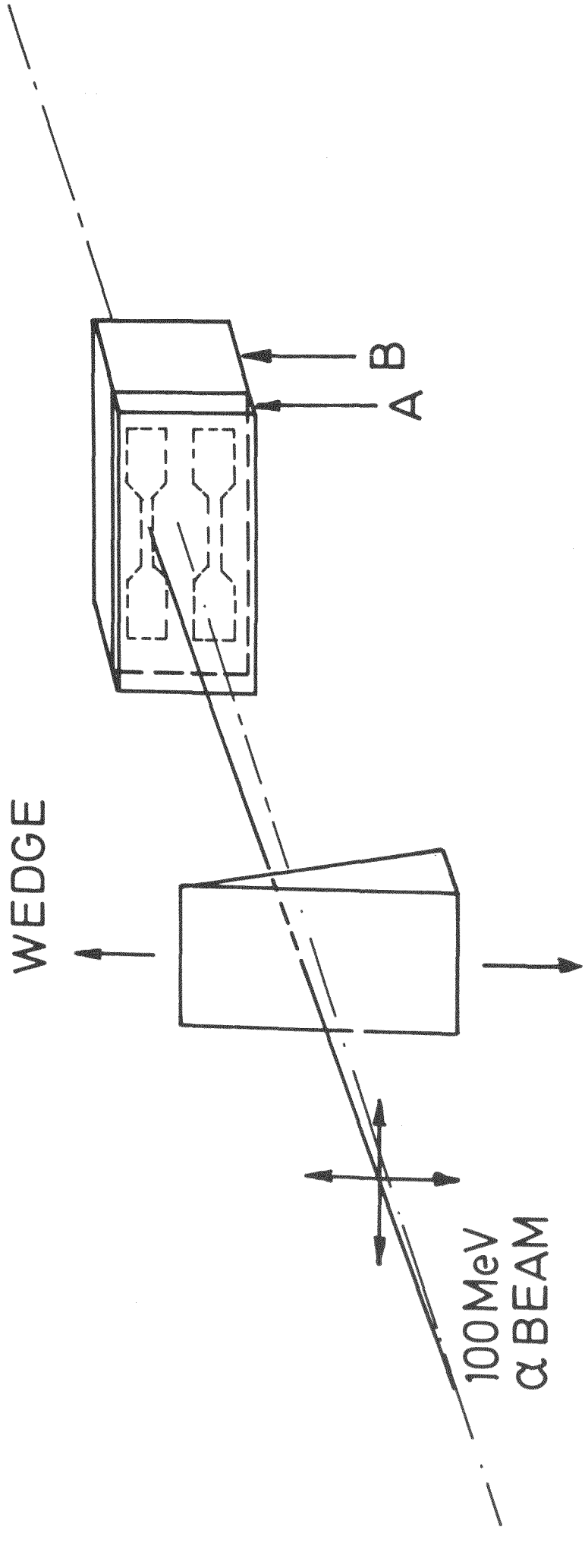

Figure 3: He implantation arrangement.

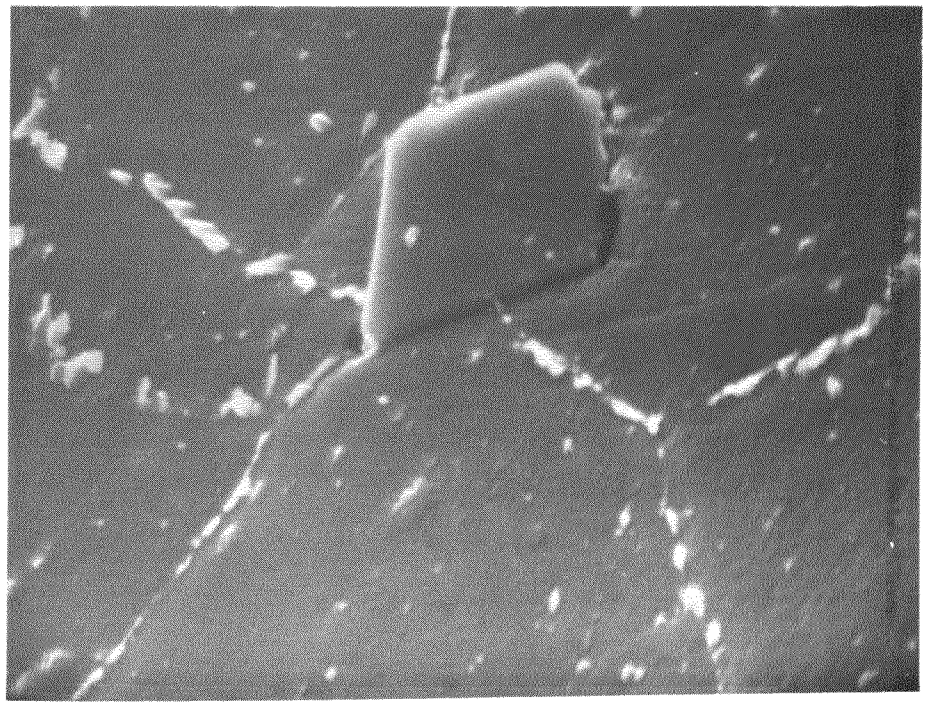

Figure 4: Surface of a polished and deep-etched specimen in the standard condition (SEM 5000X).

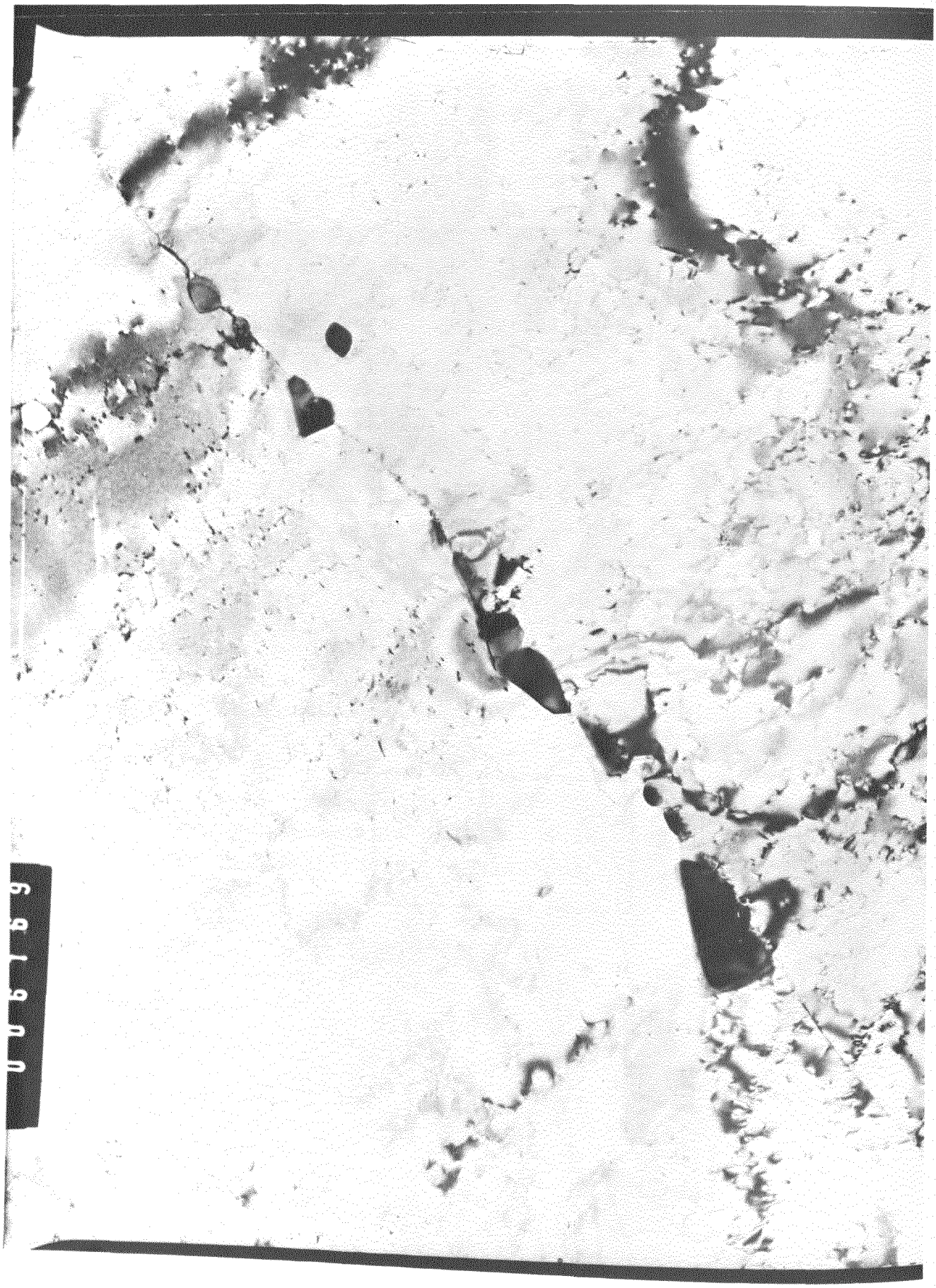

Figure 5: Material in the standard condition (TEM 60000X).

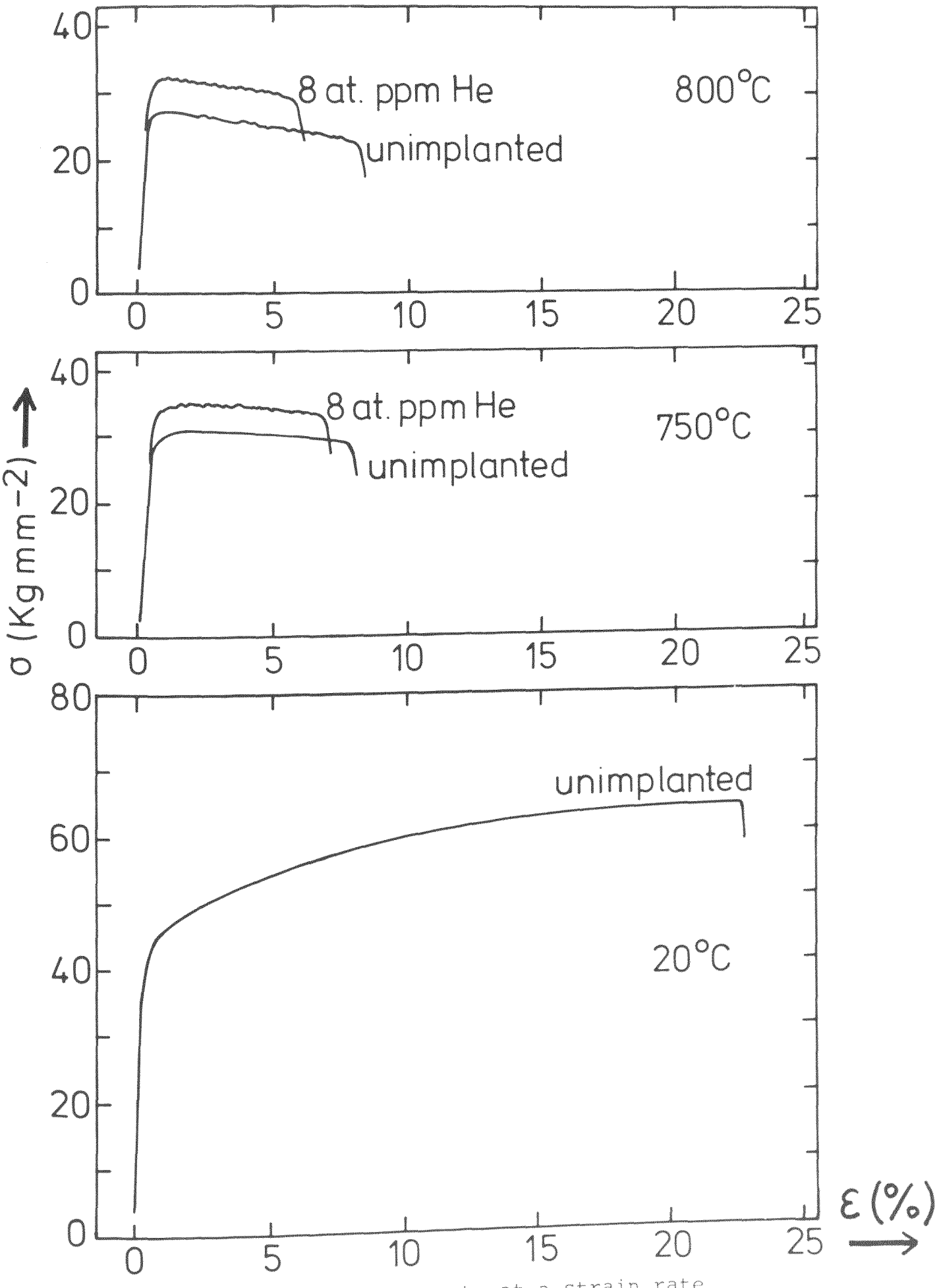

Figure 6: Tensile machine tests at a strain rate $\dot{\varepsilon} = 1.5\ 10^{-4}\ sec^{-1}$.

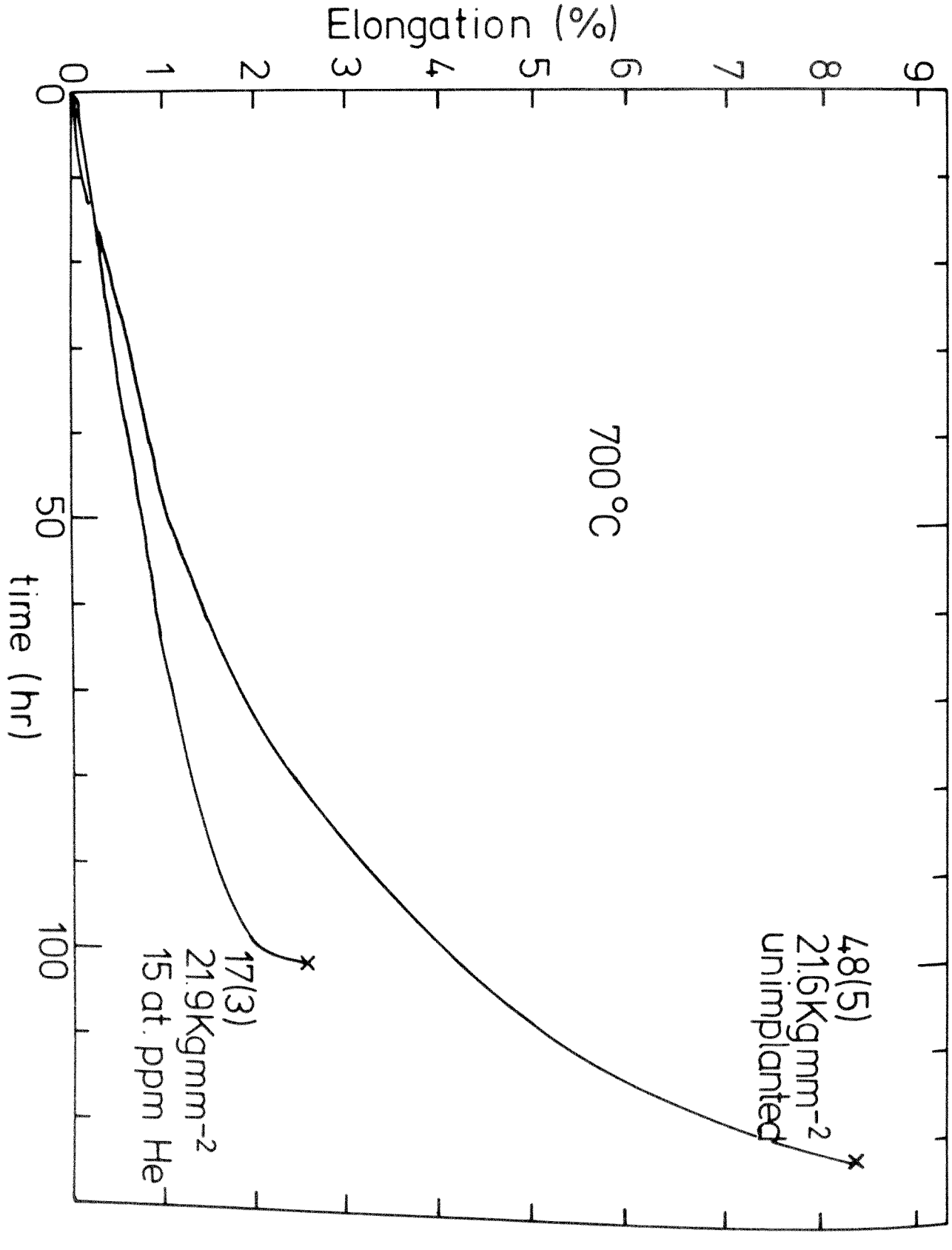

Figure 7: Typical creep curves (specimens # 48 and # 17, Table III).

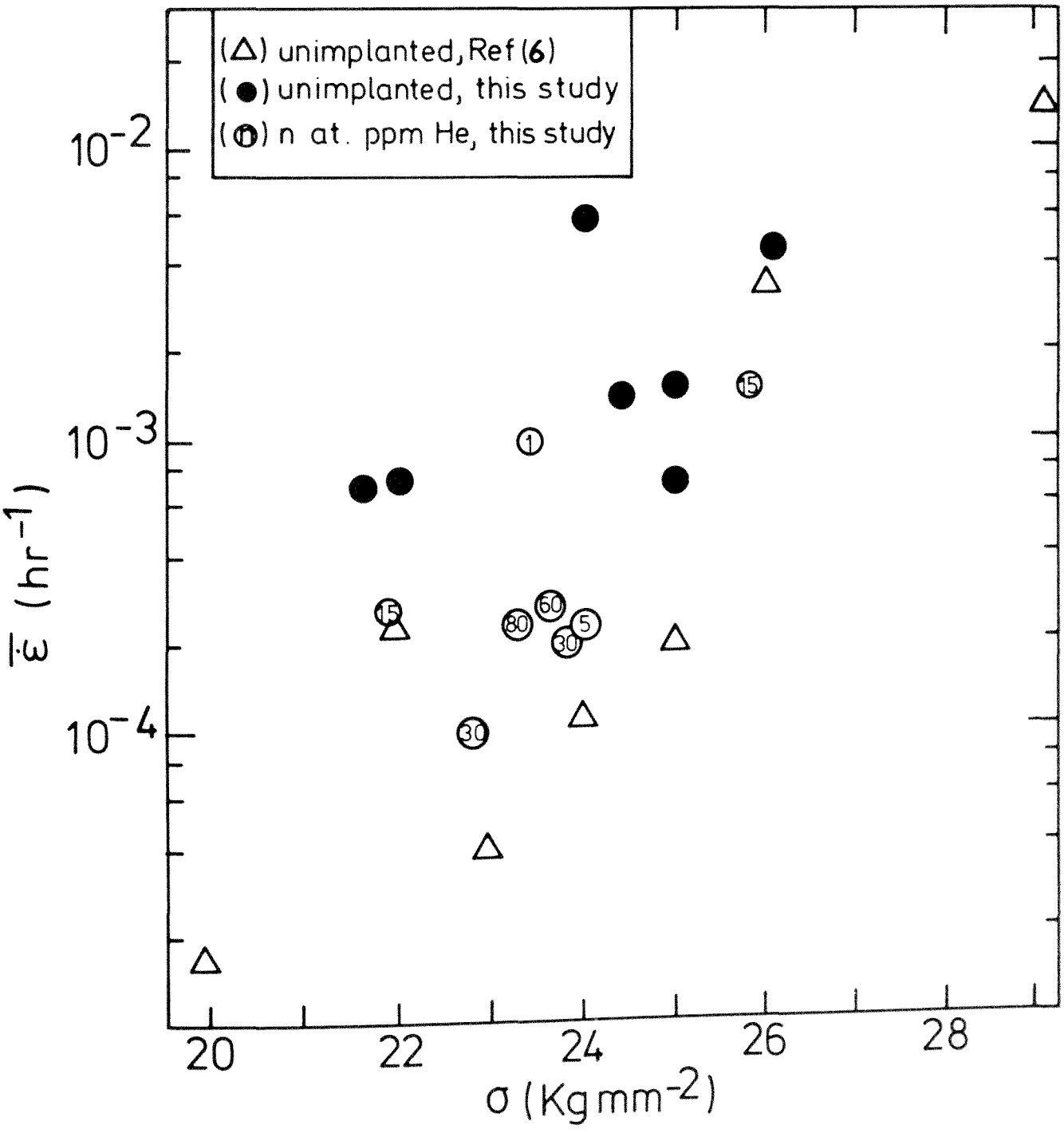

Figure 8: Average strain rate $\dot{\bar{\varepsilon}}$ as a function of the creep stress for specimens tested at 700°C.

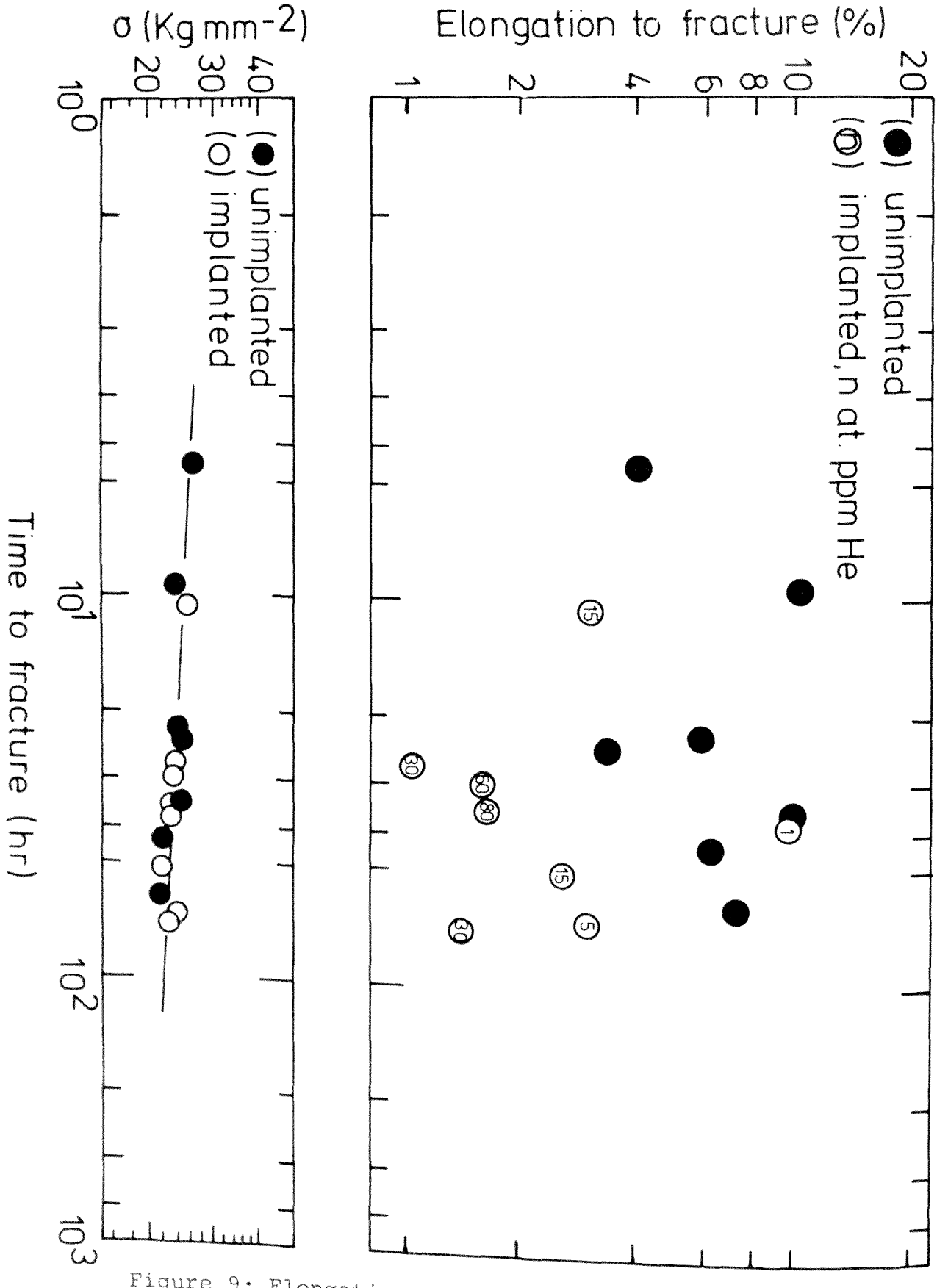

Figure 9: Elongation to fracture and creep stress as a function of the time to fracture at 700°C.

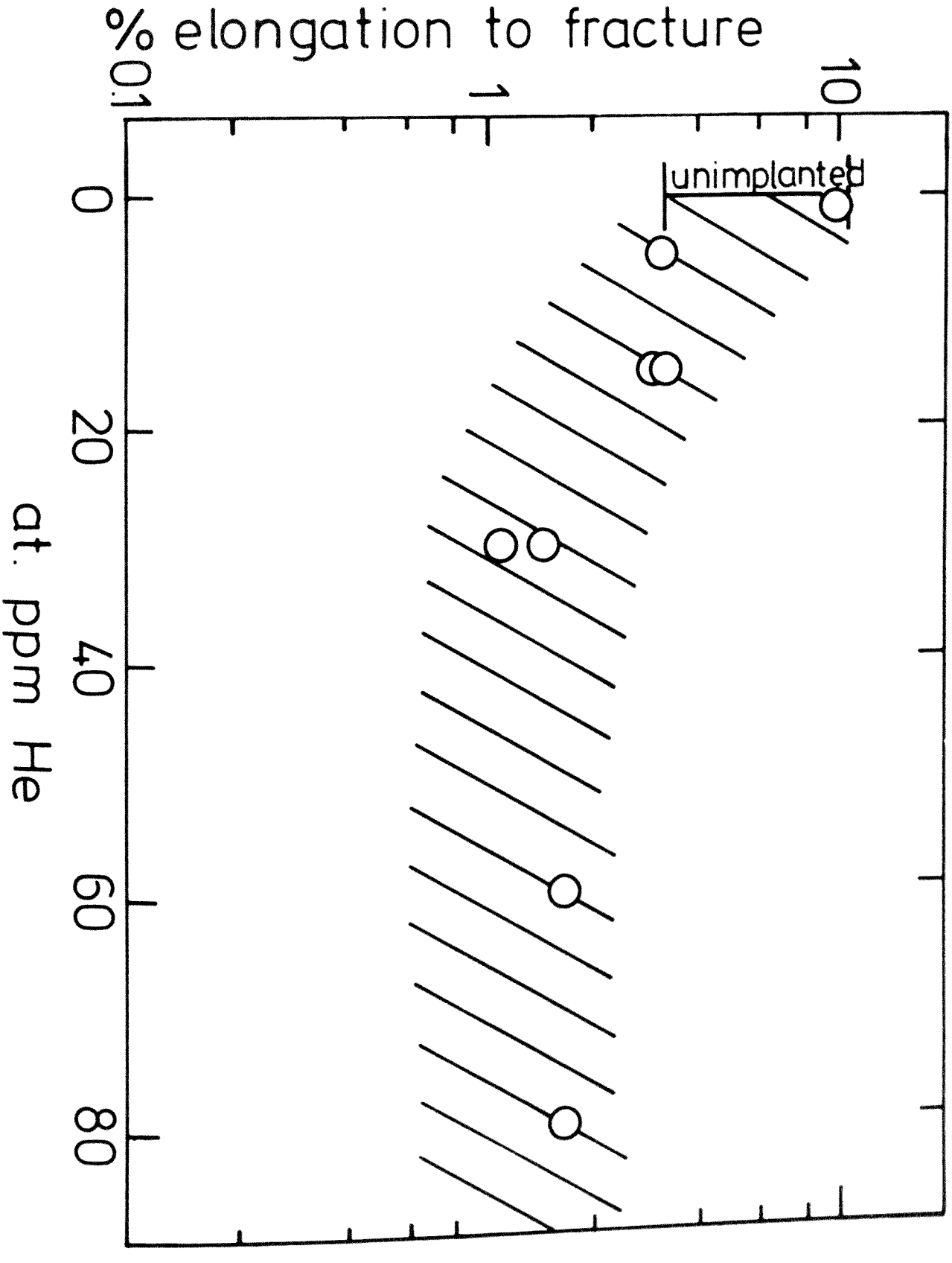

Figure 10: Effect of He content on the creep elongation to fracture at 700°C.

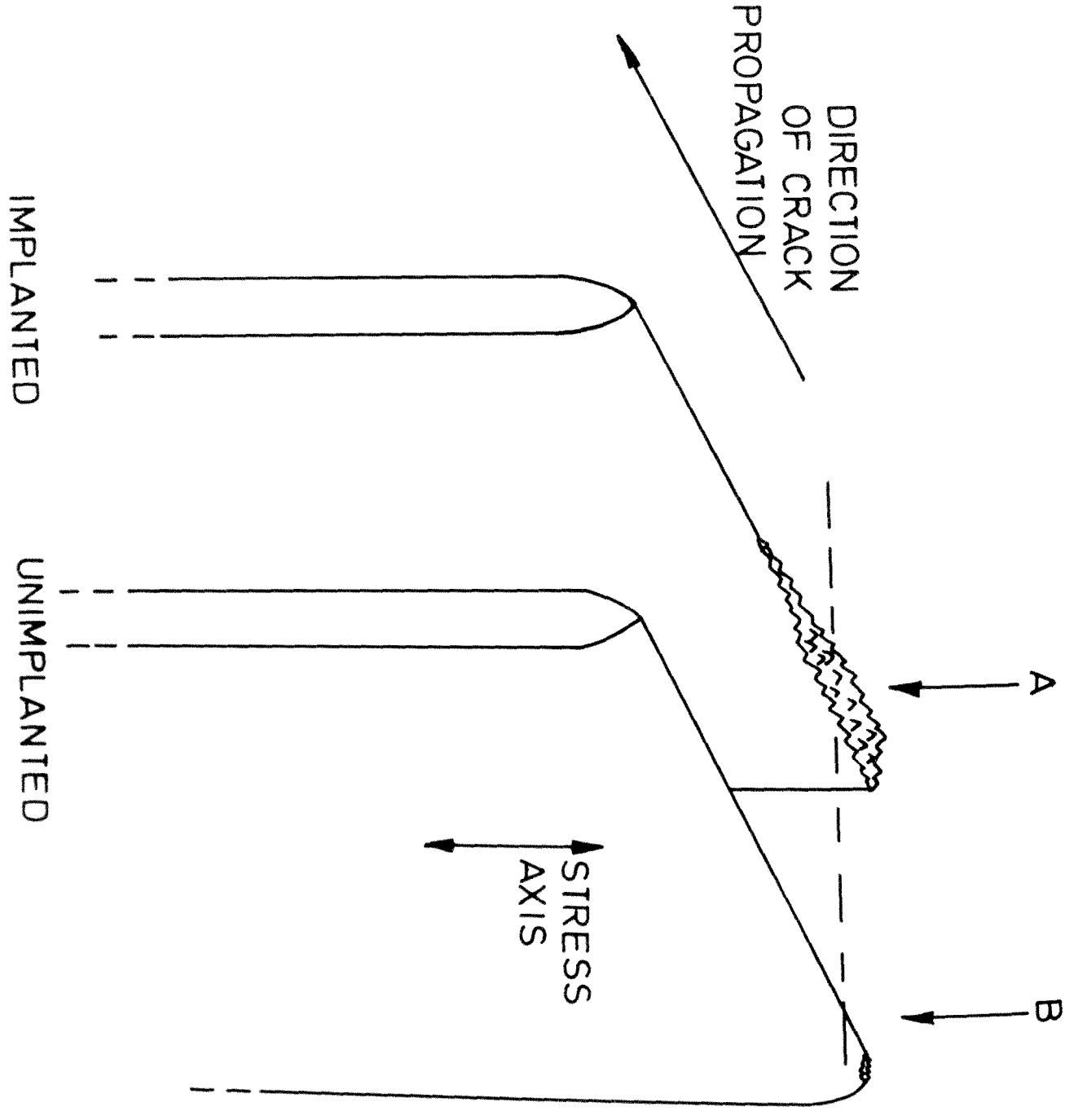

Figure 11: Fracture morphology of implanted and unimplanted specimens (schematic).

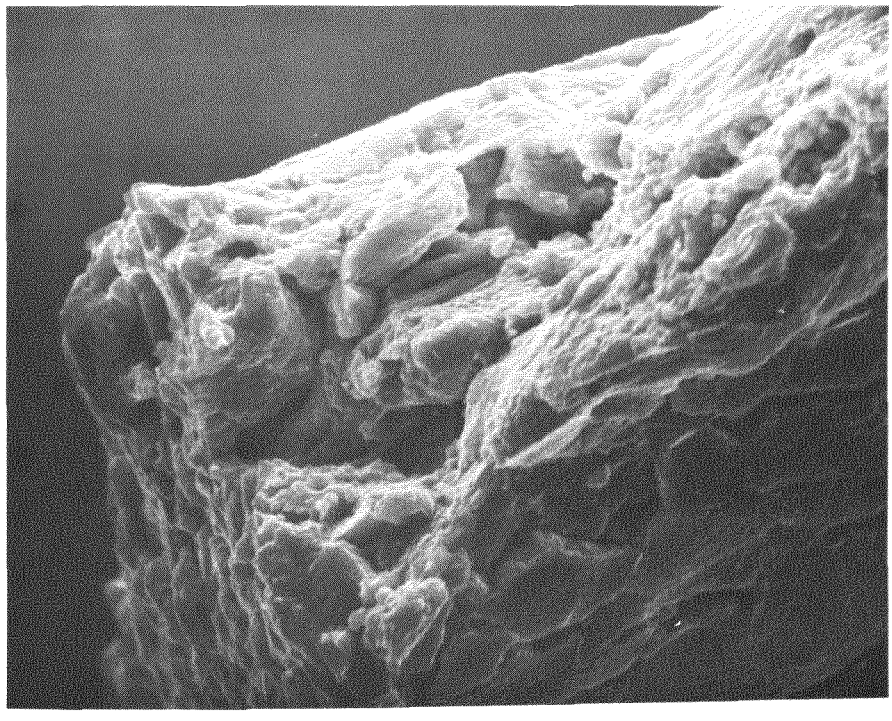

Figure 12: Region where the fracture initiated in an unimplanted specimen (# 48, Table III) tested at 700°C (SEM 640X).

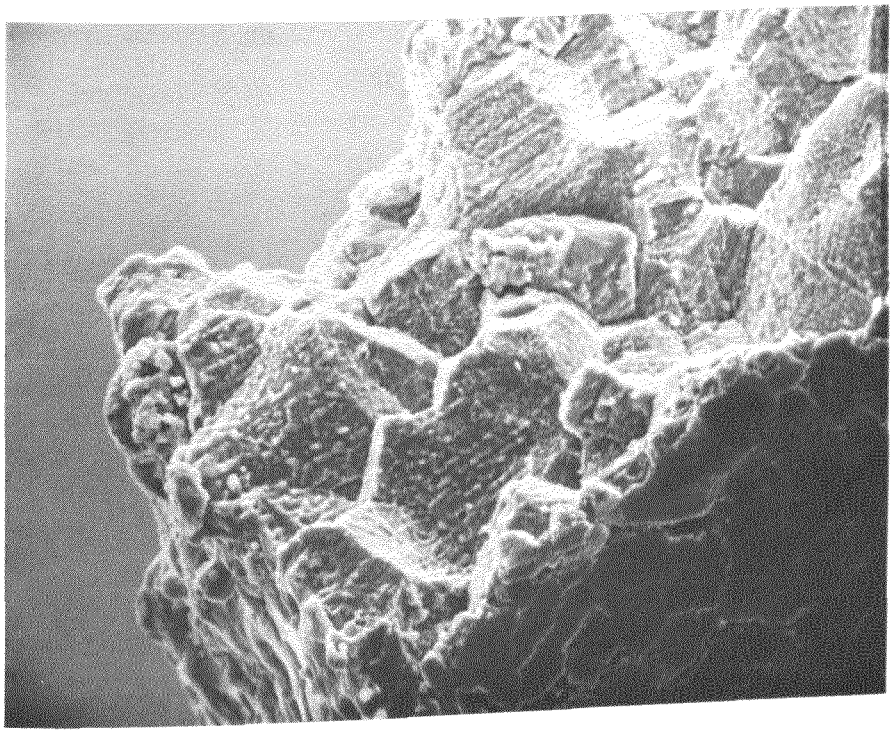

Figure 13: Region where the fracture initiated in an implanted specimen (# 17, Table III) tested at 700°C (SEM 640X).

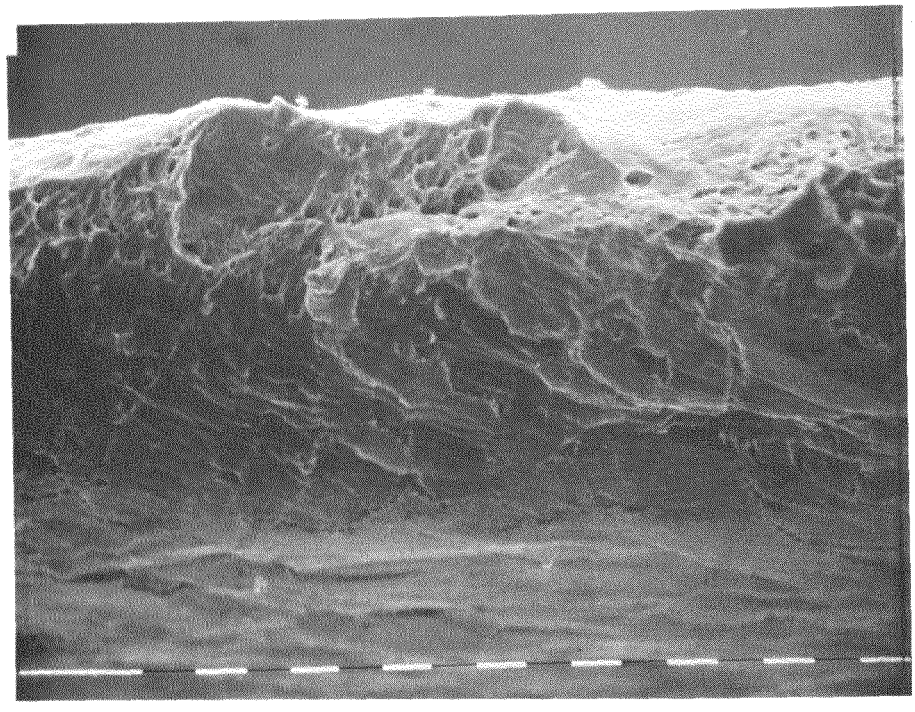

Figure 14: Appearance of the fracture surface of an unimplanted specimen (# 36, Table III) tested at 700°C as seen from B, Figure 11 (SEM 640X).

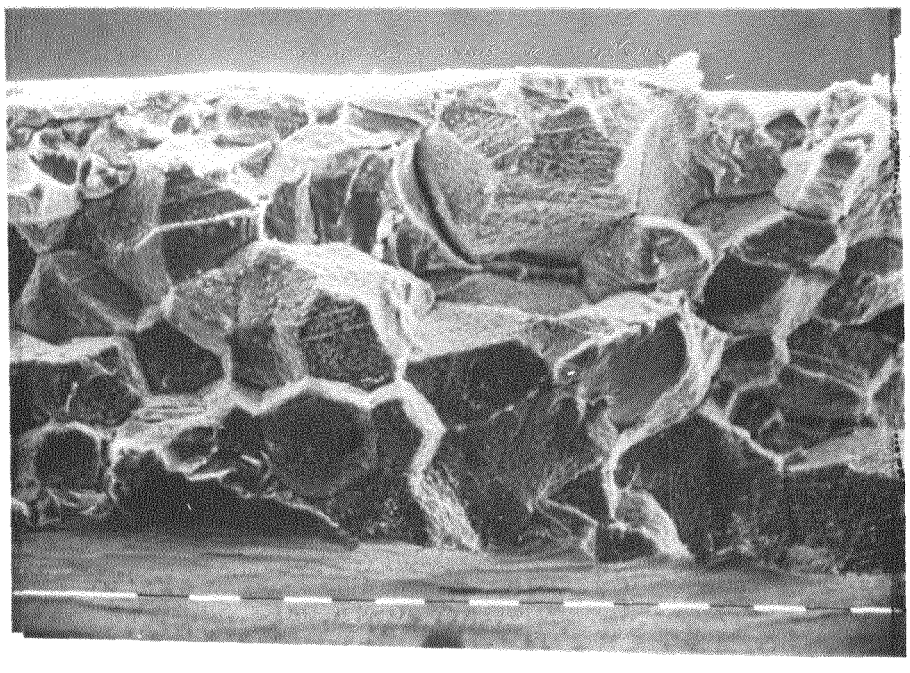

Figure 15: Appearance of the fracture surface of an implanted specimen (# 11, Table III) tested at 700°C as seen from A, Figure 11 (SEM 640X).

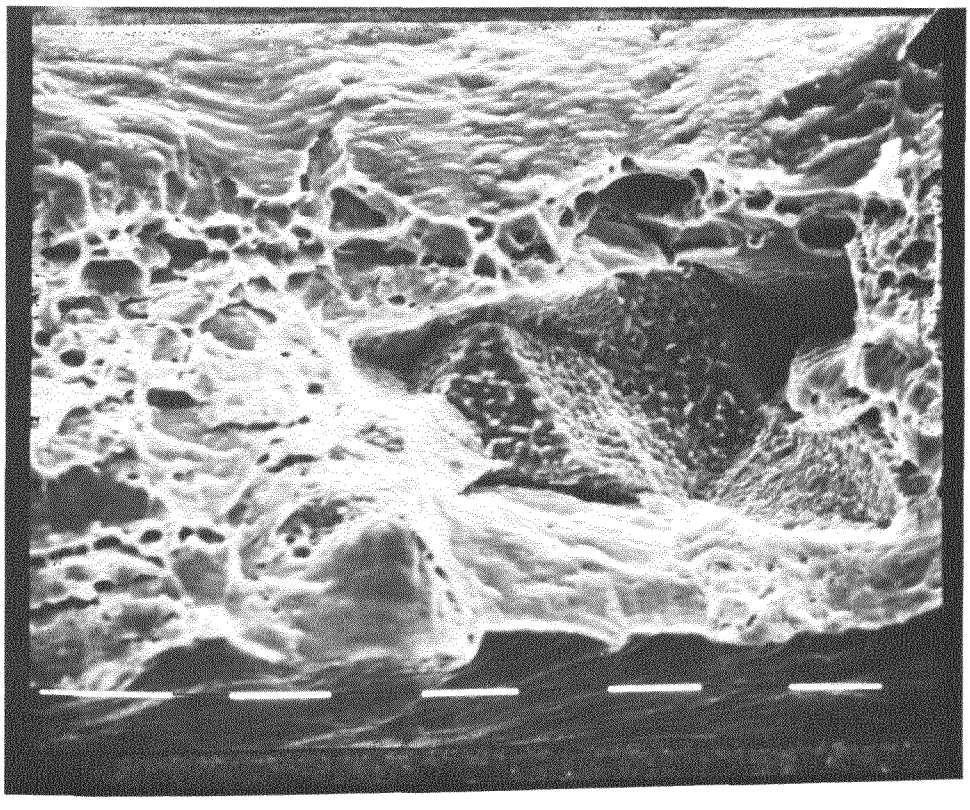

Figure 16: Region of transition from intergranular to transgranular crack propagation in an implanted specimen (# 12, Table III) tested at 700^{o}C (SEM 1250X).

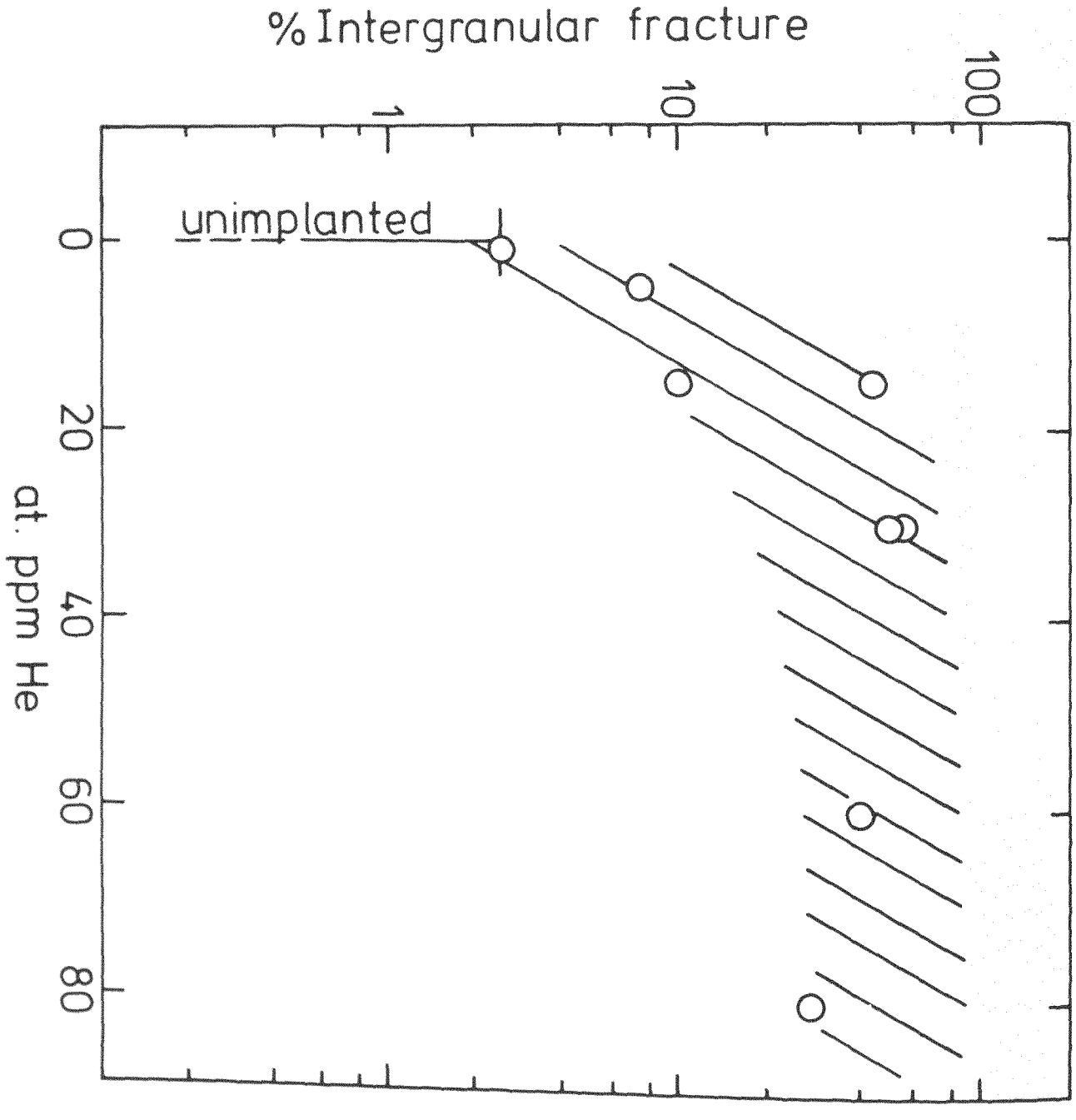

Figure 17: The magnitude % intergranular fracture as a function of He content for creep tests at 700°C.

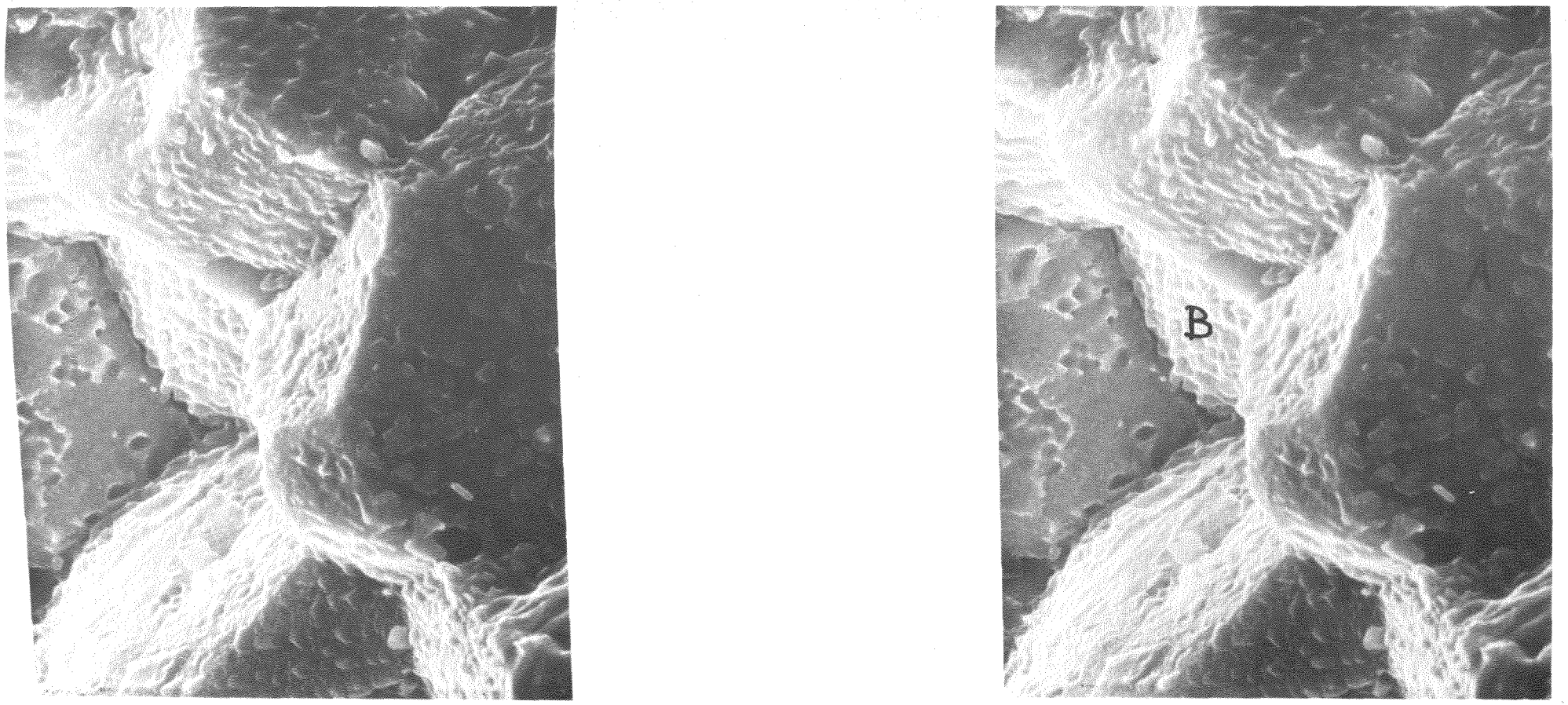

Figure 18: Stereo pair of the intergranular fracture surface of an implanted specimen (# 14, Table III) creep-tested at 700°C (SEM 5000X).

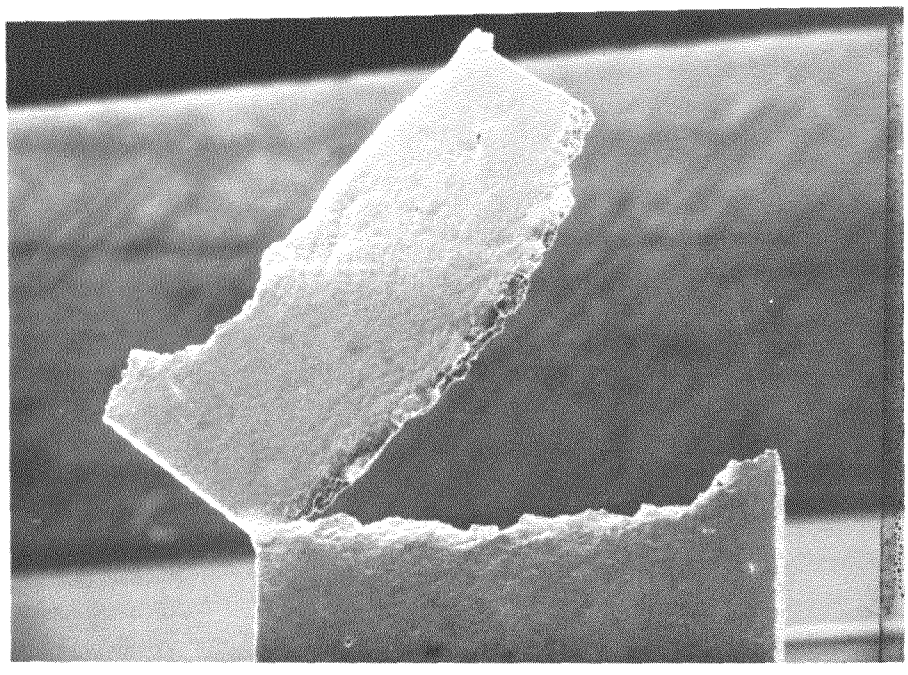

Figure 19: Side view of an implanted specimen (# 31, Table III) creep-tested at 700°C. The development of a secondary crack is uncommon (SEM 40X).

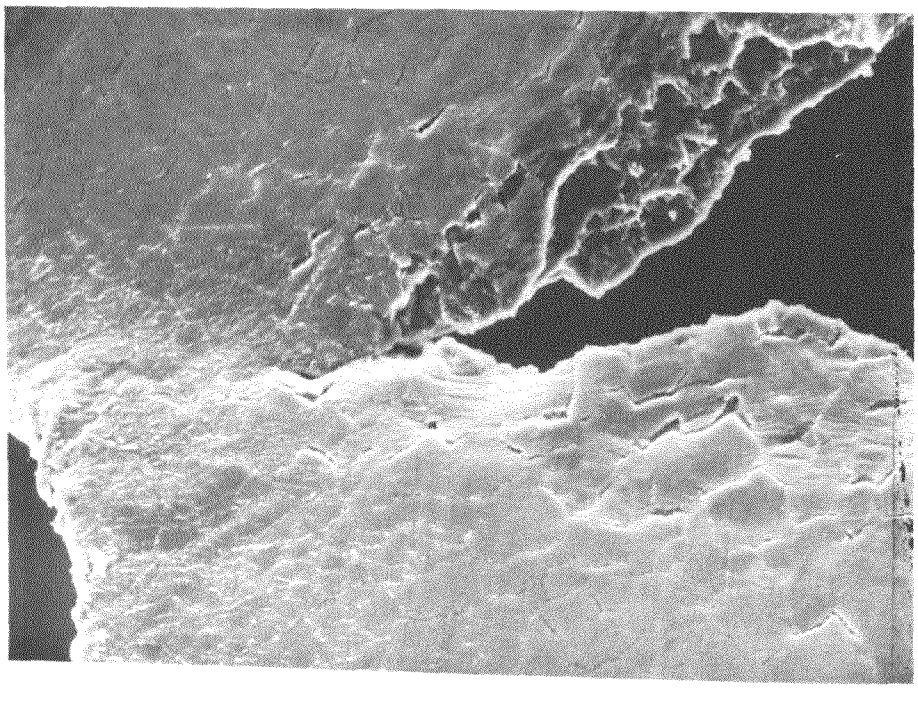

Figure 20: Advancing end of the secondary crack shown in Figure 19 (specimen # 31, Table III) (SEM 320X).

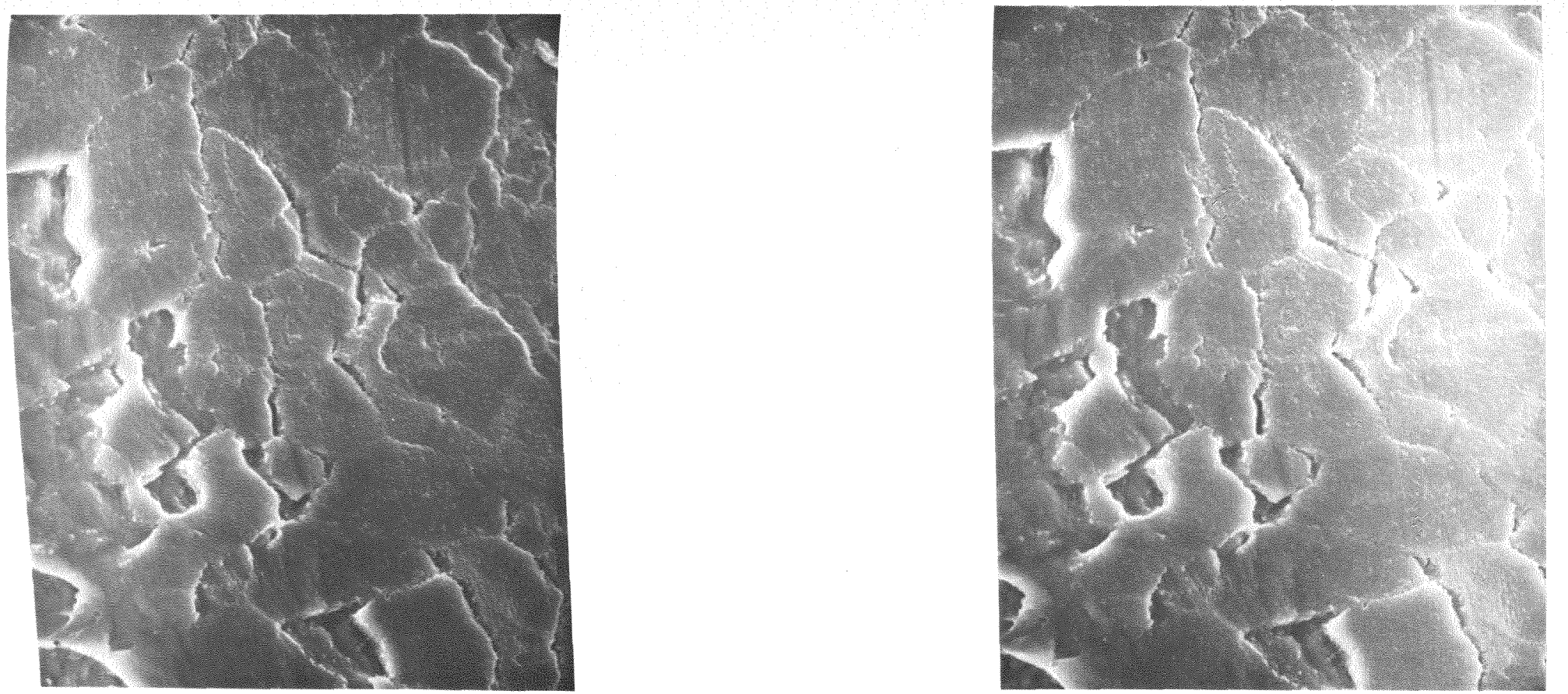

Figure 21: Stereo pair showing the shallow surface cracks that appear near the main fracture crack of an unimplanted specimen (# 48, Table III) tested at 700°C (SEM 640X).

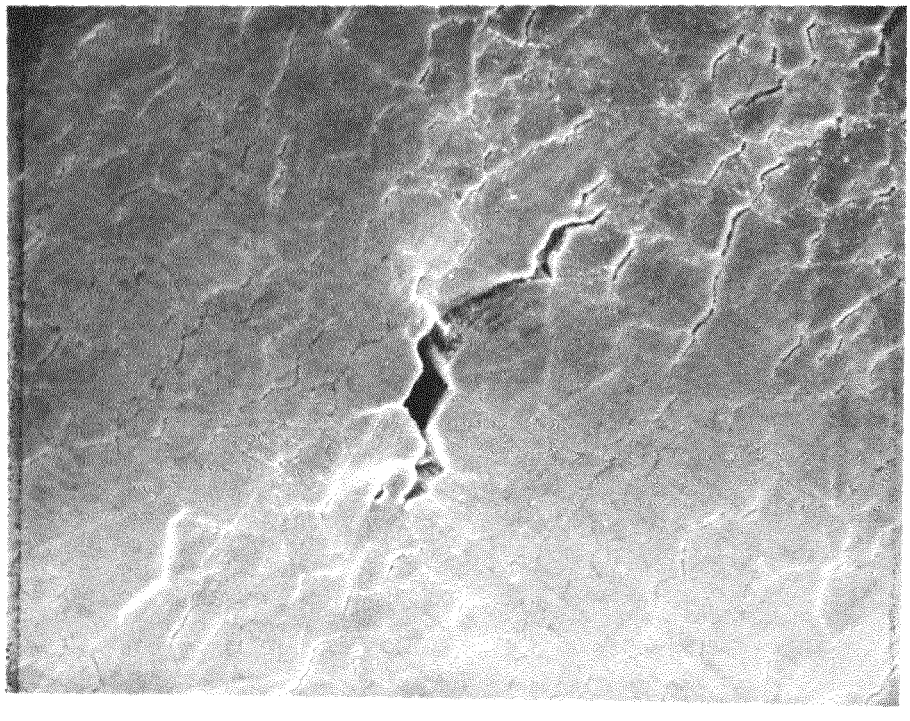

Figure 22: Enlargement of a crack visible as a short black line in the upper part of Figure 19 (SEM 320X).

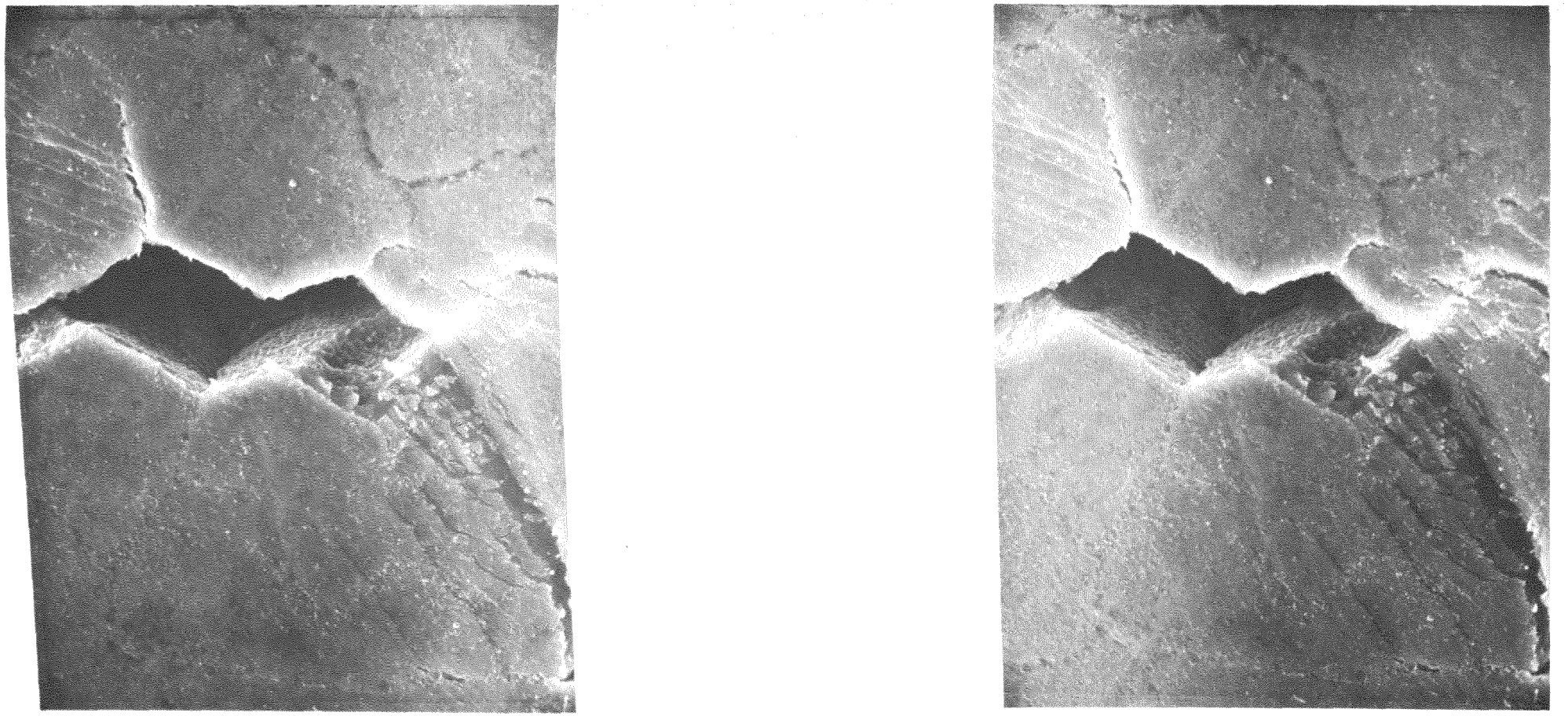

Figure 23: Stereo pair, further enlargement of Figure 22 (SEM 125OX).

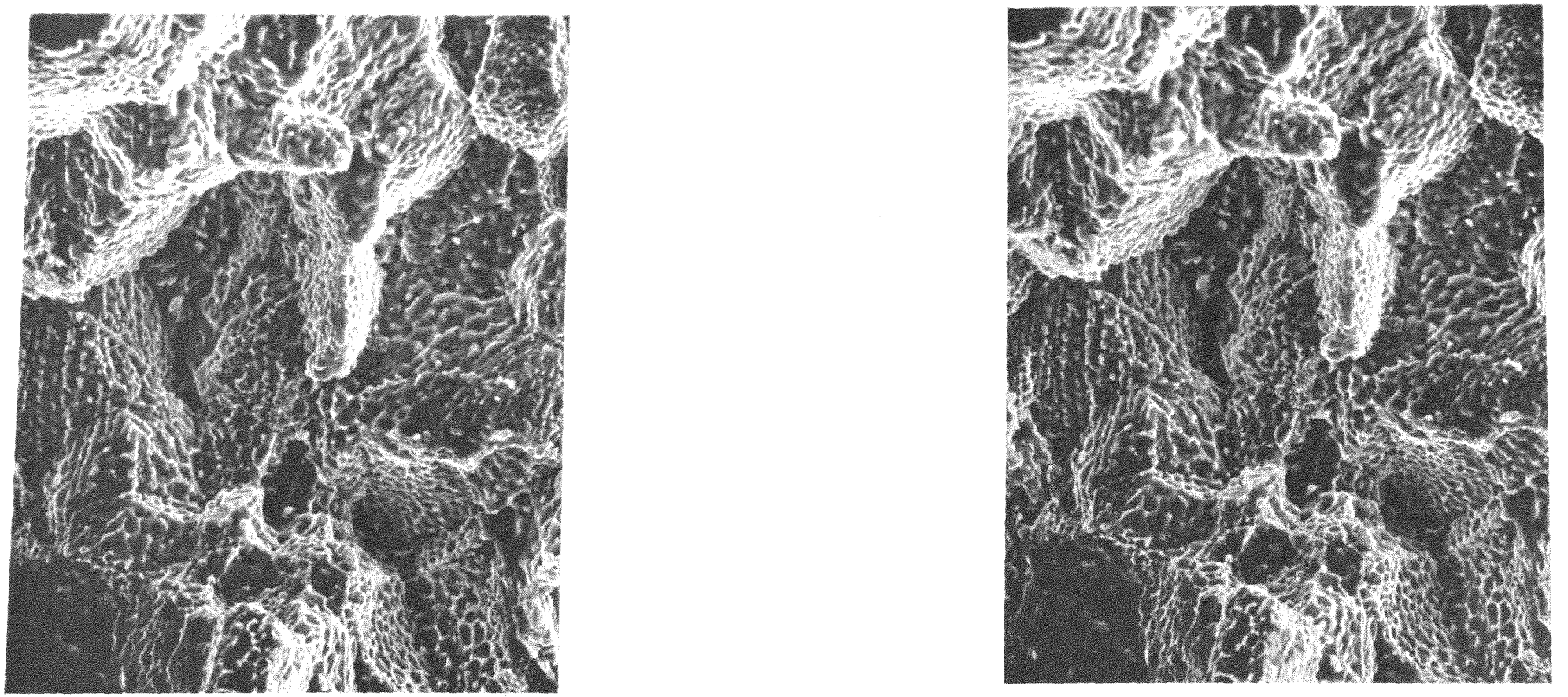

Figure 24: Stereo view of the intergranular fracture of an implanted specimen (# 18, Table III) creep-tested at 800°C (SEM 1250X).

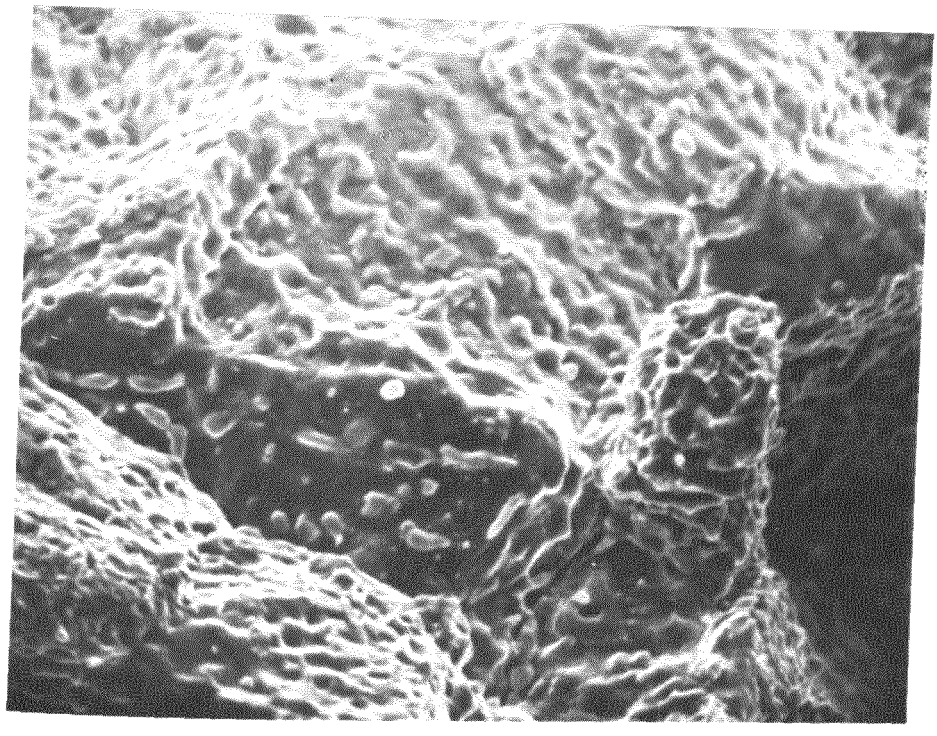

Figure 25: Concave and convex features present at the exposed grain boundaries after creep at 800^{o}C (# 18, Table III) (SEM 5000X).

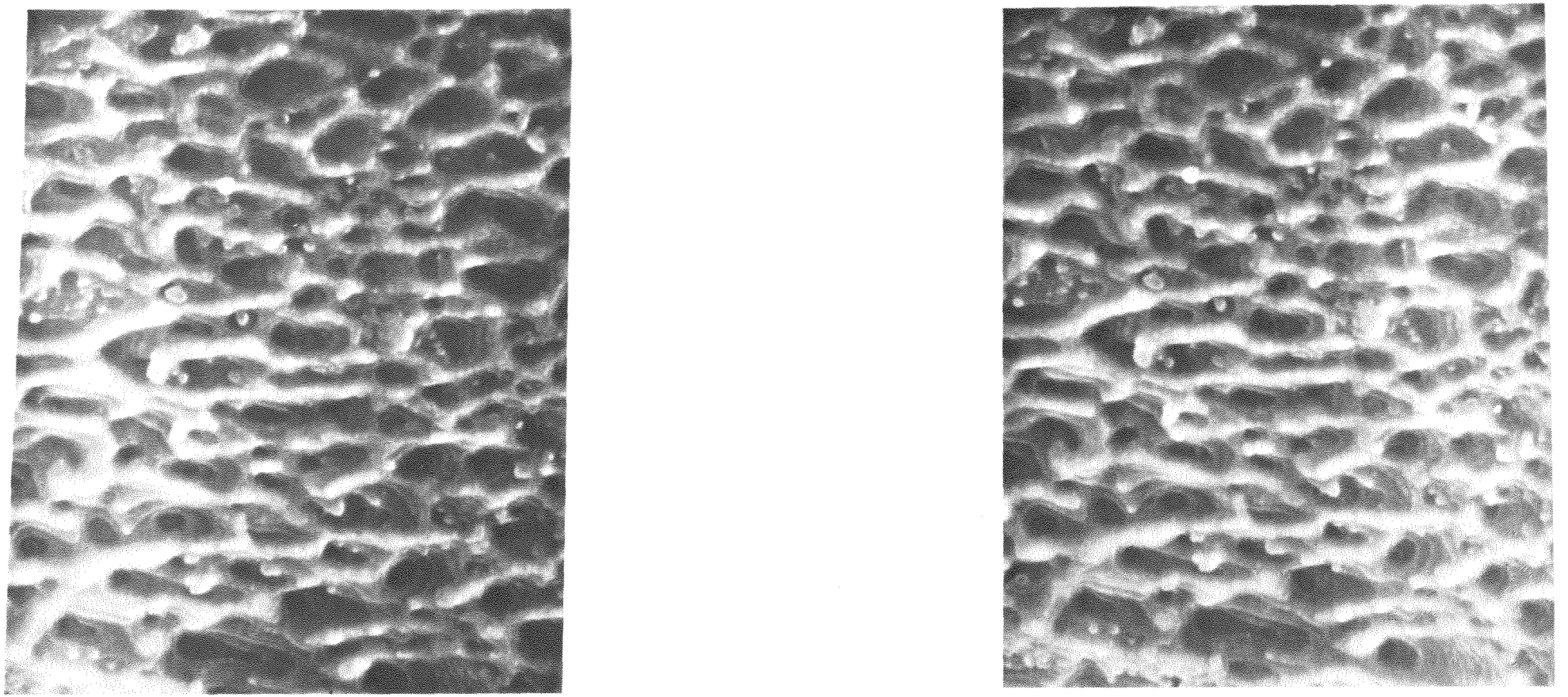

Figure 26: Stereo pair of the intergranular fracture surface of an implanted specimen (# 15, Table III) tested at 800°C, showing Cr-rich precipitates within cavities (SEM 5000X).

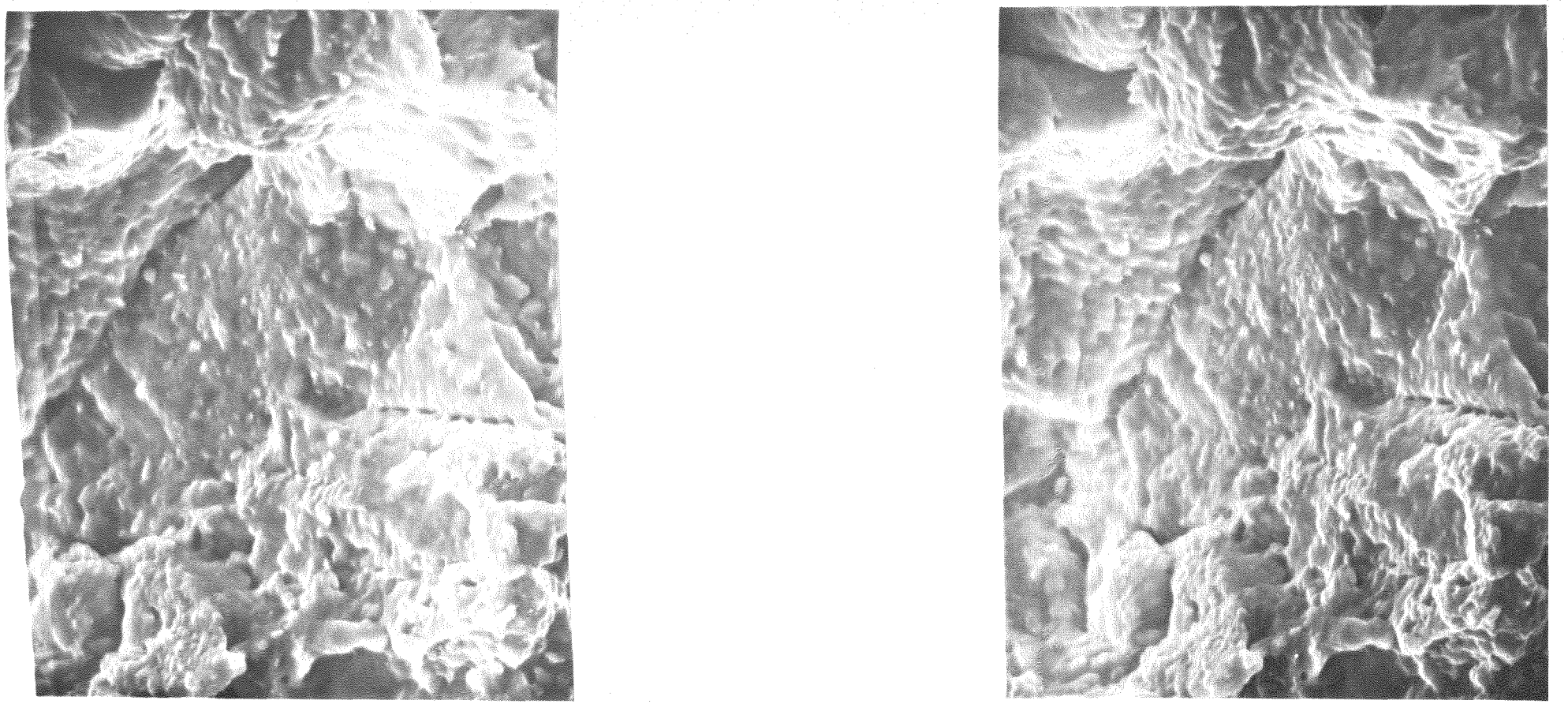

Figure 27: Stereo view of a row of cavities appearing on the intergranular fracture surface of an implanted specimen (# 38, Table III) tested at 800°C (SEM 2500X).

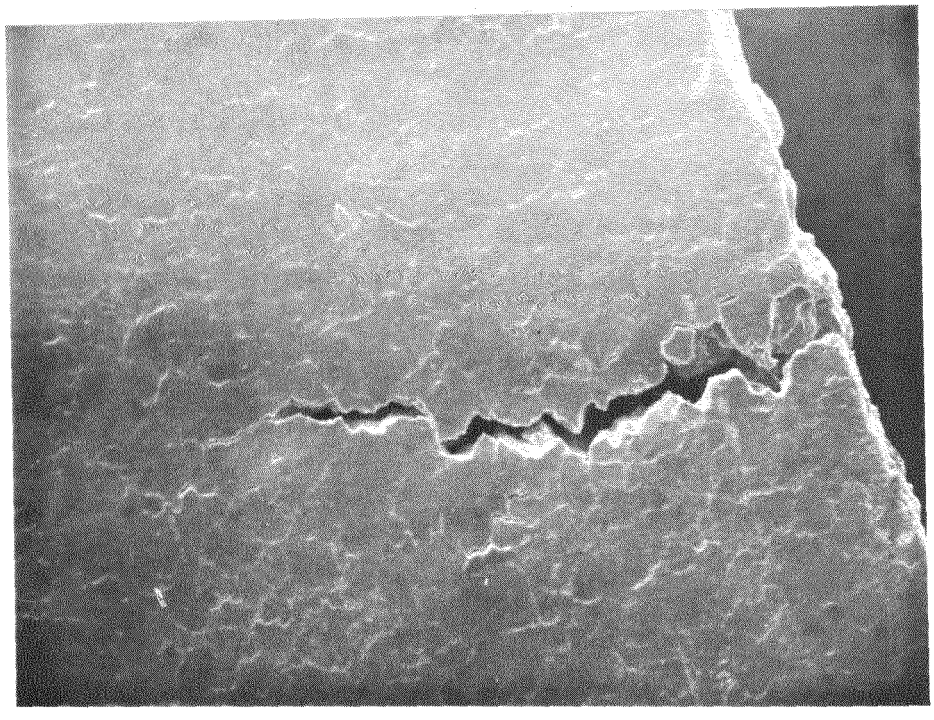

Figure 28: Secondary crack developed on the side of an implanted specimen (# 38, Table III) creep-tested at 800°C (SEM 320X).

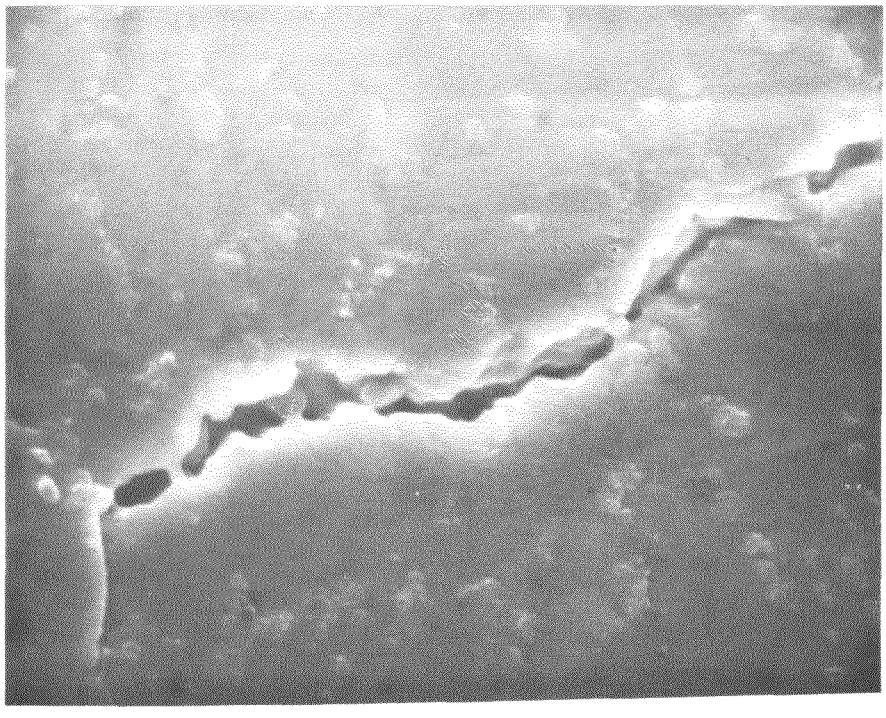

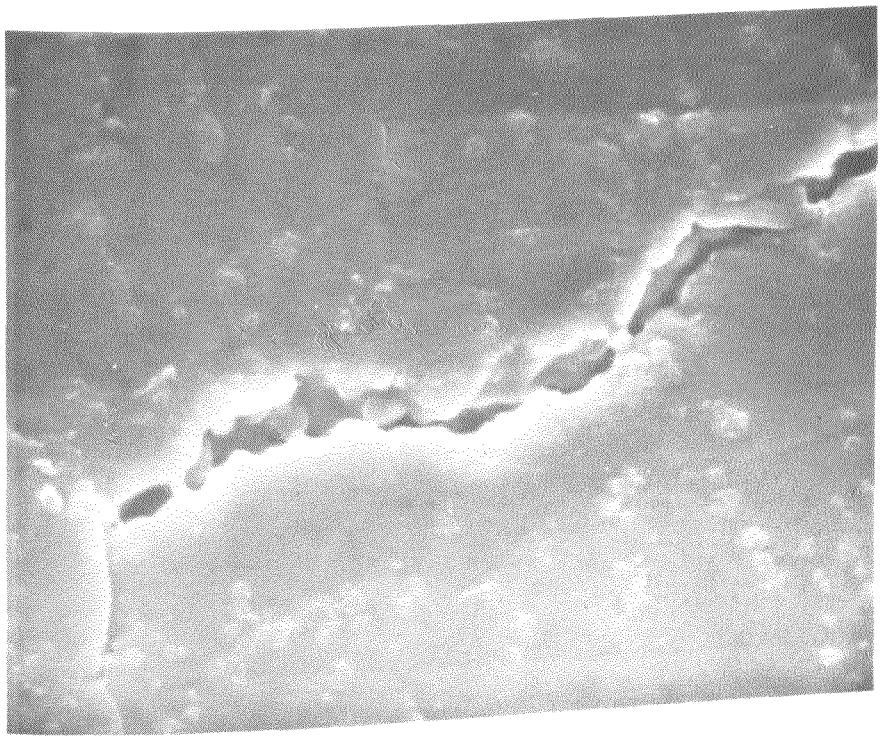

Figure 29: Stereo enlargement of Figure 28 (SEM 5000X).

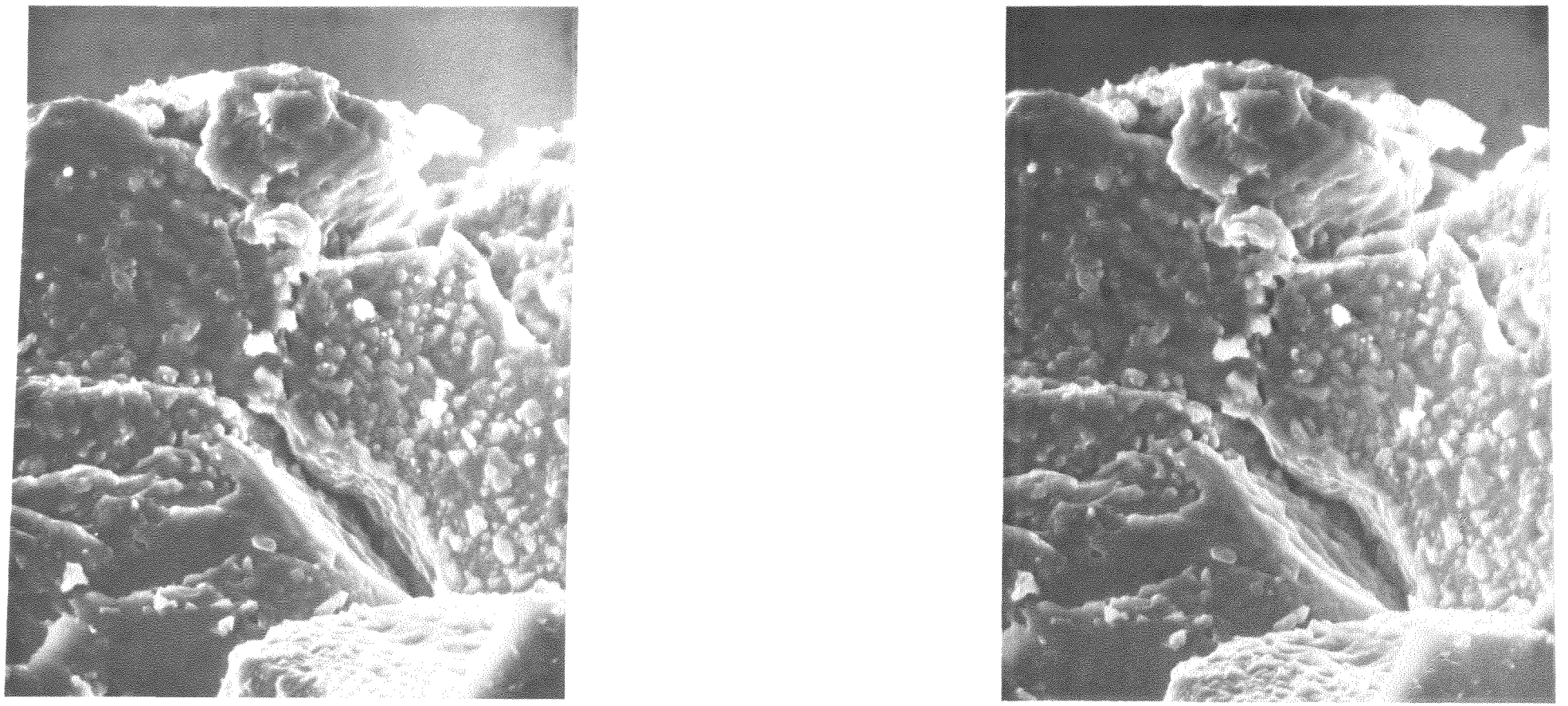

Figure 30: Stereo view of the intergranular part of the fracture of an implanted specimen (Table II, 800°C) tensile-tested at $\dot{\varepsilon} = 1.5\ 10^{-4}\ sec^{-1}$.

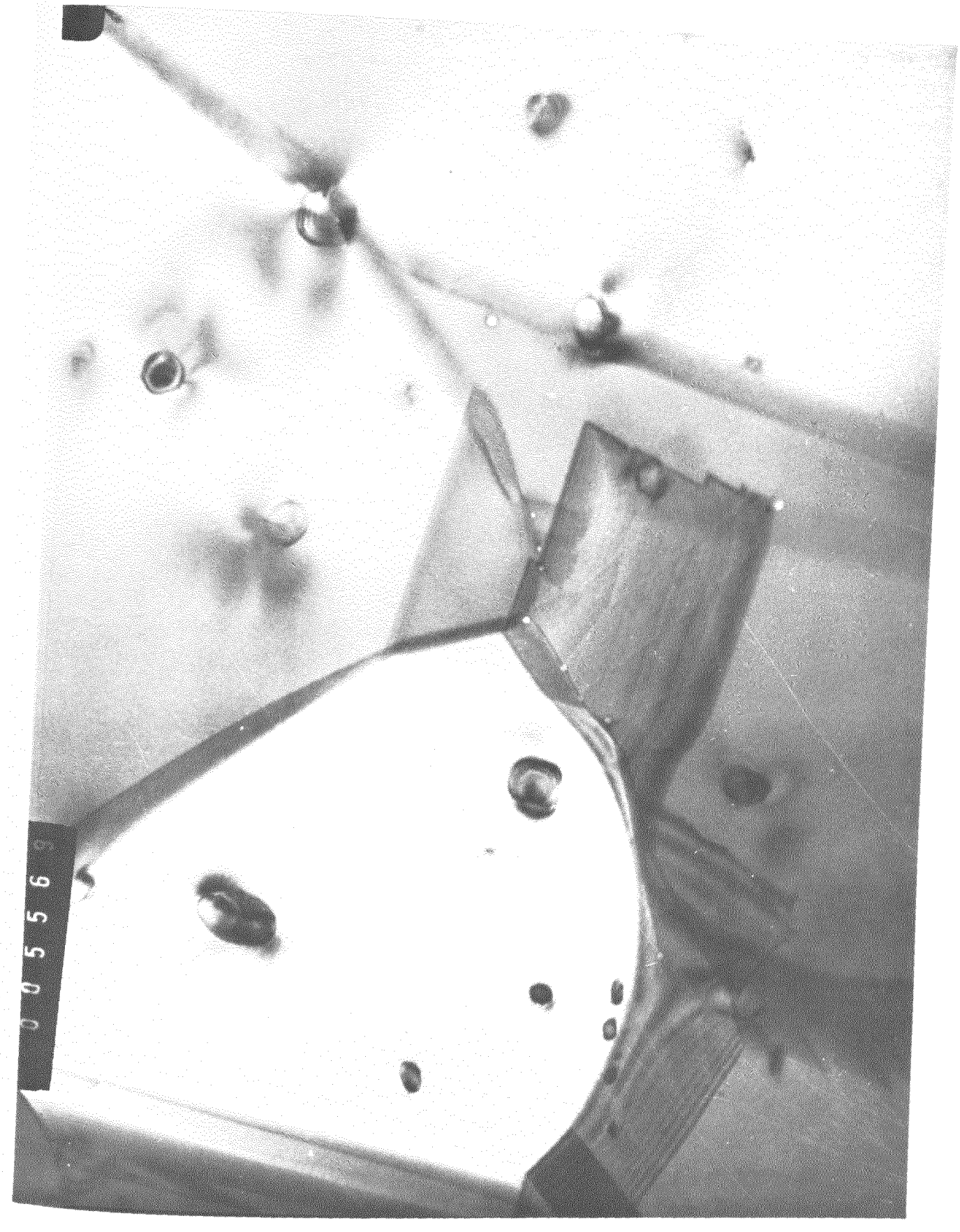

Figure 31: Helium bubbles present in a specimen containing 100 at ppm He and annealed for 1 hr at 900°C in the absence of stress (TEM 75000X).

Figure 32: Helium bubbles associated with a grain boundary precipitate and with dislocations in the matrix. Specimen containing 30 at ppm He and annealed at 1000°C in the absence of stress (TEM 120000X).

Figure 33: Helium bubbles associated with grain boundary precipitates in an implanted specimen (# 38, Table III) creep-tested at 800°C.

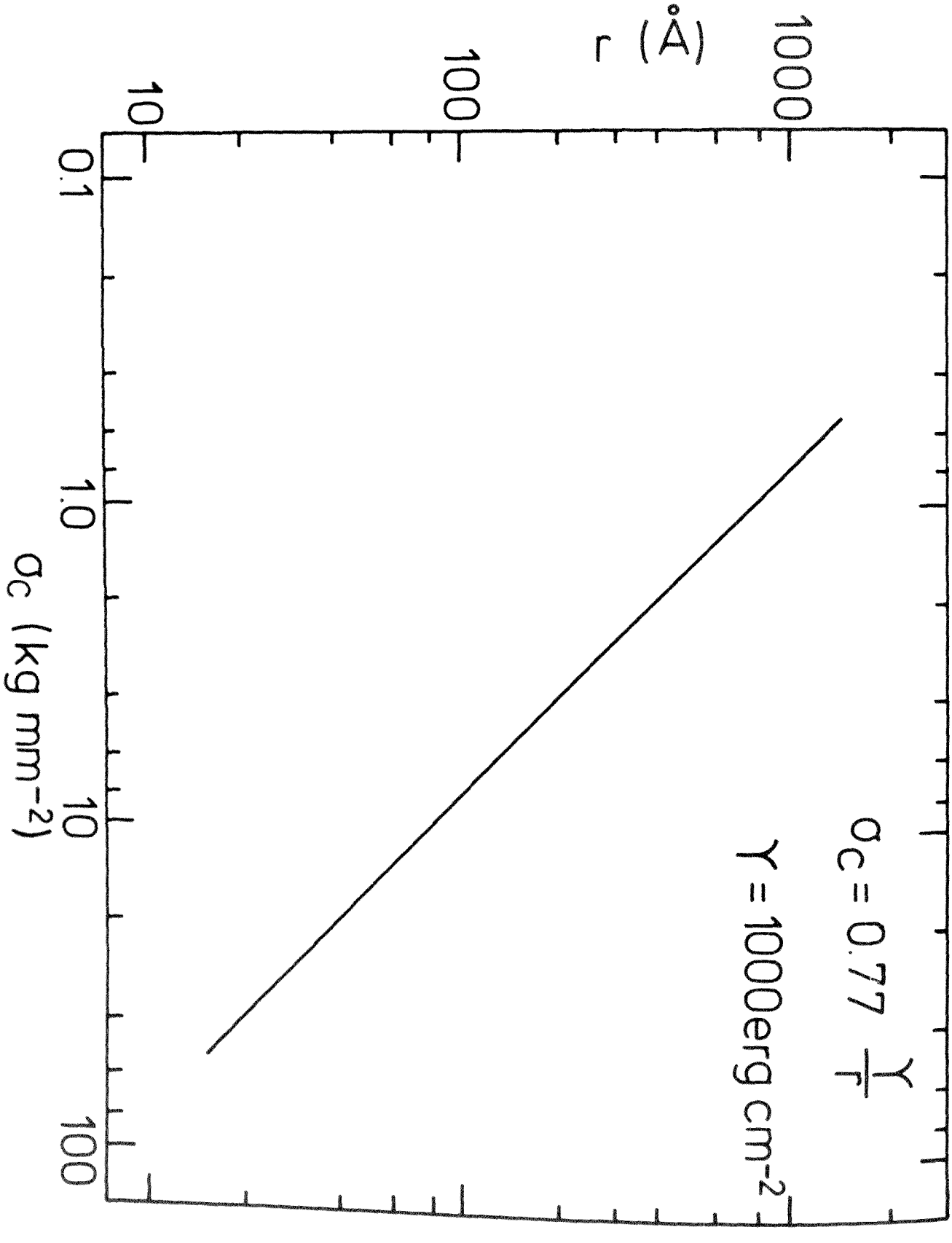

Figure 34: Critical radius-stress relationship.